Phytomedicine 148 (2025) 157451

Contents lists available at ScienceDirect

Phytomedicine

journal homepage: www.elsevier.com/locate/phymed

Original Article

Chelidonine-induced inhibition of FBP1 disrupts M2 macrophage polarization and attenuates breast cancer

Kaili Liu [a], Jianli Li [a], Zhiwei Sun [a], Yuheng Sun [a], Xuerui Zhang [a], Yang Sui [a], Zhongyuan Qu [a,*], Xiang Zou [b,*]

[a] College of Pharmacy, Harbin University of Commerce, Harbin, China
[b] Pharmaceutical Engineering Technology Research Center, Harbin University of Commerce, Harbin, China

ARTICLE INFO

Keywords:
Macrophage polarization
Chelidonine
Breast cancer
Single-cell transcriptomics
FBP1

ABSTRACT

Background: Chelidonium majus l., a traditional herbal medicine listed in the *Pharmacopoeia of China* (2025), has remarkable anticancer properties. Chelidonine (CHE), its primary bioactive alkaloid, can inhibit the proliferation of breast cancer (BC) cells; however, whether its antitumor effect in BC is mediated through regulating M2 macrophage polarization remains unexplored.

Purpose: To investigate the effect of CHE on M2 macrophage polarization in BC and to identify key molecular targets and pathways involved in its immunomodulatory effects.

Methods: The effect of CHE on tumour progression was evaluated *in vivo* using a 4T1 BCE mouse model. In addition, the effects of CHE on M2 macrophage polarization were investigated both *in vitro* and *in vivo* via immunofluorescence and Western blotting. Coculture assays were conducted to elucidate the mechanism by which CHE exerts antiproliferative and antimetastatic effects through the inhibition of M2 macrophage polarization. An integrated analysis of network pharmacology, single-cell, and bulk RNA-seq data was performed to identify potential molecular targets of CHE in the suppression of M2 macrophage polarization. Molecular docking, Western blotting, and ELISA were utilized for target validation to elucidate the roles in M2 macrophage polarization.

Results: CHE effectively impeded tumour progression in BC mice. Both *in vitro* and *in vivo* experiments demonstrated that CHE significantly inhibited M2 macrophage polarization, as evidenced by the altered expression of key polarization markers, including CD86, CD206, Arg-1, and CD11c. Under coculture conditions, CHE disrupted the mitochondrial membrane potential and compromised membrane integrity in BC cells, triggering pyroptosis via activation of the NLRP3/Caspase-1/GSDMD signaling axis. Additionally, CHE attenuated the epithelial–mesenchymal transition (EMT) process, thus reducing the migratory and invasive capacities of BC cells. An integrated analysis of network pharmacology, single-cell, and bulk RNA sequencing data revealed FBP1 as a potential molecular target through which CHE suppresses M2 macrophage polarization. Molecular docking studies revealed a relatively strong binding affinity between CHE and FBP1. Experimental validation further confirmed that CHE downregulated the expression of FBP1 and its downstream target p-STAT3 in macrophages, thereby inhibiting M2 polarization.

Conclusions: CHE might suppress M2 polarization and tumour progression by targeting FBP1. These findings highlight its potential as a therapeutic agent in immunotherapy and BC treatment.

Introduction

Breast cancer (BC) is the most prevalent malignancy worldwide, with its global burden steadily increasing over the past several decades (Arnold et al., 2022). Contemporary therapeutic strategies for BC include surgery, neoadjuvant chemotherapy, adjuvant chemotherapy, radiation therapy, immunotherapy, and molecular targeted therapy (Waks and Winer, 2019). Despite significant advancements in these medical approaches, challenges such as high recurrence rates, limited efficacy in metastatic cases, and drug resistance remain substantial hurdles in clinical management (Park et al., 2022). These limitations have prompted researchers to explore alternative therapeutic strategies,

* Correspondence.
E-mail addresses: qiuqiuqu@163.com (Z. Qu), zouxiang@hrbcu.edu.cn (X. Zou).

https://doi.org/10.1016/j.phymed.2025.157451
Received 19 June 2025; Received in revised form 3 October 2025; Accepted 21 October 2025
Available online 25 October 2025

including natural compounds derived from traditional Chinese medicine (TCM), which offer potential for holistic and innovative treatment approaches (Qu et al., 2025).

Chelidonium majus l. (CM), a traditional herbal medicine belonging to the Papaveraceae family, has been traditionally used in Chinese medicine for its analgesic, antitussive, and detoxifying properties (Chinese Pharmacopoeia Commission, 2025). Clinically, CM is often combined with *Corydalis yanhusuo* to form a commonly used herbal pair in traditional Chinese medicine to serve as an adjuvant treatment for tumours (Yu, 2010). Among its active constituents, chelidonine (CHE) has attracted significant attention due to its notable anticancer properties (Zou et al., 2014). The anticancer drug Ukrain, with CHE as its primary active component, has shown significant therapeutic potential across a range of malignancies, including bladder, breast, pancreatic, rectal, and colorectal cancers. Its efficacy has been demonstrated both as a standalone therapy and in combination with standard chemotherapeutic agents or ionizing radiation (Ernst and Schmidt, 2005). Ukrain was evaluated by the National Cancer Institute (USA) as part of its drug screening program under the designation NSC 631570 (Panzer et al., 2000). Furthermore, the use of Ukrain as a cancer immunostimulant has been shown to enhance the immune function of cancer patients, accompanied by clinical improvements in disease progression (Nowicky et al., 1991). These findings align with the traditional use of CM in alleviating tumour-associated symptoms (Yu, 2010), providing a strong rationale for further investigation into the molecular mechanisms and therapeutic potential of CHE. Recent studies have demonstrated that CHE suppressed cell proliferation and induced M phase arrest and mitotic catastrophe in BC cells by regulating the AKT/FOXO3/FOXM1 axis (Li et al., 2024). Moreover, CHE has been shown to reverse doxorubicin resistance in BC by inducing pyroptosis via the NLRP3/Caspase-1/GSDMD signaling pathway (Zou et al., 2025a). CHE could effectively overcome the resistance of MCF-7/ADR cells to ADR by targeting the PDGFRb/PI3K/Akt axis (Zou et al., 2025b). Beyond BC, CHE exhibits broad-spectrum anticancer activity, including inducing apoptosis in pancreatic cancer cells via the p53-GADD45A pathways (Jang et al., 2021), inhibiting gefitinib-resistant non-small cell lung cancer cells via the EGFR–AMPK signaling pathway (Xie et al., 2020), and enhancing the efficacy of lenvatinib in hepatocellular carcinoma (Hou et al., 2019). However, most current studies focus on the direct antitumour effects of CHE, with limited research exploring its role in modulating the tumor immune microenvironment (TME), particularly through macrophage polarization.

TME consists of cancer cells and their neighboring stromal, endothelial, and immune cells, plays a pivotal role in cancer initiation, progression, and therapeutic resistance (Deepak et al., 2020). TME influences key processes such as proliferation, angiogenesis, apoptosis inhibition, immune suppression, and drug resistance (Elhanani et al., 2023). Among the cellular components within the TME, macrophages stand out as key contributors, exhibiting functional plasticity and being broadly classified into two phenotypes: M1 macrophages, which demonstrate antitumour properties, and M2 macrophages, which promote tumour growth and metastasis (Gou et al., 2021). The majority of tumor-associated macrophages (TAMs) in the TME exhibit an M2-like phenotype, contributing to immune suppression, enhanced angiogenesis, and tumour progression. For example, cytokines such as interleukin 4 (IL-4), interleukin 10 (IL-10), and transforming growth factor β (TGF-β) can drive M2 polarization, which is closely associated with an immunosuppressive TME and poor clinical outcomes in BC patients (Gou et al., 2021). Modulating macrophage polarization within the TME has thus emerged as an attractive therapeutic strategy for improving immune responses and enhancing the efficacy of anticancer therapies. However, effective therapeutic options that can reshape the immune landscape of the TME remain limited. These findings underscore the need to explore bioactive natural products with immunomodulatory potential, particularly those capable of restoring antitumour immunity through macrophage reprogramming.

In this study, we focused on the potential of CHE as a novel therapeutic agent for BC, particularly because of its effects on macrophage polarization within the TME. By integrating network pharmacology, single-cell RNA sequencing (scRNA-seq), bulk transcriptomic data and experimental validation, we aimed to elucidate the molecular mechanisms by which CHE exerts its antitumour effects. This study not only expands our understanding of the immunomodulatory functions of CHE but also provides a scientific foundation for the development of CHE-based therapeutic strategies for BC prevention and treatment.

Materials and methods

Cell cultures

4T1-luc cells were obtained from Shanghai Meixuan Biological Science and Technology Co., Ltd., and cultured in RPMI 1640 medium supplemented with 10 % fetal bovine serum (FBS) and 1 % penicillin-streptomycin (PS). The E0771 cell line was purchased from Jingyuan Bio and maintained in DMEM supplemented with 10 % FBS and 1 % PS. Similarly, the murine monocyte/macrophage cell line RAW264.7, provided by the Engineering Research Center on Natural Antineoplastic Drugs, Ministry of Education, was cultured in DMEM containing 10 % FBS and 1 % PS. All cell lines were maintained in a humidified incubator at 37 °C with 5 % CO_2 and 95 % air.

Animal handling and experimental design

animals

Female BALB/c mice (8 weeks old, 20–22 g) were obtained from Liaoning Changsheng Biotechnology Co., Ltd. (License No. SCXK[Liao] 2020–0001). The mice were housed in a well-ventilated facility under controlled conditions: a constant temperature of 25 ± 1 °C, relative humidity of 50 ± 10 %, and a 12-hour light/dark cycle. Bedding was changed every two days. All experimental procedures were approved by the Ethics Committee for Experimental Animals at Harbin University of Commerce (Approval No. HSDYXY-2024032).

Establishment of BC models and intervention strategies

After a one-week acclimatization period, female BALB/c mice were subcutaneously injected with 1×10^6 4T1-luc cell into the right axillary region. Once the solid tumors reached a volume of 50–100 mm^3, the mice were randomly divided into five groups, with ten mice in each group. The experimental groups were as follows: the model group (treated with distilled water), the cyclophosphamide (CTX) group, which received CTX (H22022673, Tonghua Maoxiang Pharmaceutical Co., Ltd.) at a dose of 10 mg/kg daily, and three CHE-treated groups, which were administered CHE (DST220428-079, ≥98 % purity, obtained from Shanghai Yuan Ye Bio-Technology Co., Ltd.) at varying doses via daily oral gavage. CHE doses were selected based on literature (Hou et al., 2019) and preliminary experiments: the high dose (CHEH, 20 mg/kg) was confirmed to exert significant antitumor efficacy without hepatotoxicity/nephrotoxicity (assessed via HE staining), while medium (CHEM, 10 mg/kg) and low (CHEL, 5 mg/kg) doses were set as 50 % and 25 % of the high dose to explore dose-response relationships. A control group consisting of non-tumor-bearing mice received distilled water. Tumor dimensions were measured every three days using calipers, and both the length (l) and width (W) were recorded for each measurement. Tumor volume (V) was calculated using the formula: $V = (l \times W^2)/2$ (Li et al., 2021). After 14 days of treatment, various parameters were assessed. Blood samples were collected from the orbital sinus of all mice, and spleen, lung, and tumor tissues from each group were harvested and weighed following standard protocols.

In vivo imaging of tumor progression in small animal models

Mice were anesthetized with isoflurane (R510-22-16, Shenzhen

Rayward Life Technology Co., Ltd.) and placed on a temperature-controlled imaging stage to ensure physiological stability during *in vivo* imaging. To stimulate bioluminescence, d-luciferin (2 mg/100 μl, $C_{11}H_7KN_2O_3S_2$, Dalian Belgreen Biotechnology Co., Ltd.) was administered via intraperitoneal injection, following standard protocols. After 10 min under anesthesia, mice were transferred to the IVIS Lumina III system (PerkinElmer) for imaging. Bioluminescent signals were detected and recorded using optimized exposure parameters. Data acquisition and signal quantification were performed using dedicated software for *in vivo* imaging analysis.

Hematoxylin and eosin (H&E) staining

Tissue samples, including those from tumors, lungs, liver, and kidneys, were fixed in 10 % neutral-buffered formalin (202307558, Aobo Biotechnology Co., Ltd.) at room temperature for 24 hours. After fixation, the samples underwent a graded ethanol dehydration process (70 %, 80 %, 90 %, 95 %, and 100 %) and were subsequently embedded in paraffin. The paraffin-embedded tissues were sectioned into 5-μm slices and mounted on glass slides. To prepare the slides for staining, they were dewaxed in xylene and rehydrated through a descending ethanol gradient. Hematoxylin and eosin (H&E) staining was performed (H648599, Shanghai Aladdin Biochemical Technology Co., Ltd.), where hematoxylin stained nuclei blue, and eosin colored the cytoplasm pink. Following staining, the slides were dehydrated, cleared, and coverslipped for analysis. Tissue morphology and cellular details were observed under a light microscope.

Immunofluorescence (IF)

Tissue sections were fixed in 4 % paraformaldehyde at room temperature for 30 min, followed by permeabilization with 0.03 % Triton X-100 (G3068, Servicebio) at 37 °C for another 30 min. To reduce nonspecific binding, the slides were blocked using 5 % Bovine Serum Albumin (BSA) (GC305010, Servicebio) for 1 hour at 37 °C. Primary antibodies targeting Cluster of Differentiation 86 (CD86) (DF6332, Affinity) and Cluster of Differentiation 206 (CD206) (DF4149, Affinity) were applied at optimized dilutions and incubated overnight at 4 °C. After washing with Phosphate-Buffered Saline (PBS), species-specific fluorescent secondary antibodies were added and incubated for 90 min at 37 °C. Nuclei were counterstained with a working solution of 4′,6-diamidino-2-phenylindole (DAPI) (G1012, Servicebio) for 10 min at 37 °C. The slides were subsequently mounted using buffered glycerol and analyzed under a fluorescence microscope to visualize the expression of cellular markers.

Immunohistochemistry (IHC)

Tumour tissue sections were fixed in 4 % paraformaldehyde at room temperature for 30 min, followed by antigen retrieval in citrate buffer (pH 6.0) at 95 °C for 15 min. After cooling to room temperature, the sections were permeabilized with 0.1 % Triton X-100 for 10 min. To reduce nonspecific binding, slides were blocked with 10 % normal goat serum for 30 min at 37 °C. Primary antibodies against Ki67 (AF0198, Affinity) and CD31 (AF8016, Affinity) were applied at optimized dilutions and incubated overnight at 4 °C. The following day, sections were washed with PBS and incubated with HRP-conjugated secondary antibodies for 1 hour at 37 °C. After additional PBS washes, staining was developed with a DAB substrate kit (G1211, Servicebio) until optimal intensity was achieved. Nuclei were counterstained with hematoxylin for 1 min, and slides were dehydrated through graded ethanol, cleared in xylene, and mounted with neutral balsam. Stained sections were analyzed under a light microscope to evaluate marker expression.

Cell cytotoxicity assay

Cells were plated in 96-well plates and exposed to a range of CHE concentrations for 48 hours. After treatment, 10 μl of Cell Counting Kit-8 (CCK-8) reagent (K101823133EF5E, APExBIO) was added per well, followed by a 4-hour incubation at 37 °C. Absorbance at 450 nm was then measured using a microplate reader to determine cell viability.

Effect of CHE on the macrophage M2 polarization

Experimental procedure for M2 polarization of RAW264.7 macrophages

RAW264.7 cells were resuspended in serum-free DMEM at a density of 5×10^5 cells/ml and seeded into a 6-well plate. Following a 24-hour adhesion period, IL-4 (032423230328, Shanghai Biyuntian Biotechnology Co., Ltd.) was supplemented at a concentration of 20 ng/ml to induce M2 polarization.

Observation of cellular morphological changes using optical microscopy

RAW264.7 macrophages in the logarithmic phase were suspended in serum-free DMEM and seeded into a 6-well plate. After 24 hours, the supernatant was removed, and the cells were washed with PBS. M2 polarization was induced with IL-4 and incubated for 48 hours. The polarization status was assessed by optical microscopy. CHE was then administered to the M2-polarized macrophages at predetermined concentrations of 6, 12, and 24 μM, and the cells were incubated for 48 hours. After treatment, the medium was removed, and cells were rinsed with PBS to eliminate any remaining treatment agents. Cellular morphology was evaluated by optical microscopy, and representative fields were documented.

Detection of macrophage CD206 expression by fluorescence microscope

RAW 264.7 cells were cultured, grouped, and treated as outlined in Section 2.8.2. Fixation was performed using 1 ml of 4 % paraformaldehyde for 30 min, followed by permeabilization with 200 μl of 0.5 % Triton X-100 for 20 min. The cells were then blocked with 500 μl of 3 % FBS for 30 min and incubated overnight at 4 °C with 200 μl of anti-CD206 antibody (4000000538, Wuhan Abebio Science Co.). The next day, unbound primary antibody was washed off with PBS, and 200 μl of FITC-conjugated goat anti-rabbit IgG secondary antibody (A0562, Beyotime) was added. After a 1-hour incubation in the dark, nuclei were counterstained with DAPI (1 μg/ml) for 5 min. Fluorescence intensity was observed under a fluorescence microscope, with images captured from three random fields per group. Quantitative analysis was conducted using ImageJ software.

Preparation of conditioned media from RAW264.7 macrophages

RAW264.7 macrophages were polarized into the M2 phenotype as described in Section "2.8.1″. After polarization, culture supernatants were collected from both control (M0) and M2-polarized macrophage (M2), centrifuged at 1000r for 5 min to remove cell debris, and designed as conditioned media (CM). Each CM was mixed with RPMI 1640 medium (with 10 % FBS) at a 1:1 ratio and used in subsequent experimental to assess the effects of macrophage-derived factors under different polarization conditions on target cells.

Evaluation of the effect of CHE on cell proliferation of BC pretreated with CM

Cell colony formation assay

4T1 cells were seeded in 6-well plates at a density of 500 cells/ml, with 2 ml of cell suspension per well. After 24 hours, the medium was replaced with CM and cultured for another 24 hours. CHE was then administered at concentrations of 6, 12, and 24 μM for 48 hours. Following treatment, the CHE-containing medium was removed, and cells were rinsed and maintained in fresh RPMI 1640 medium, which

was replaced every 2–3 days. Cultures were continued for 15–21 days until colony formation. For analysis, colonies were fixed with 4 % paraformaldehyde, stained with 0.1 % crystal violet, and washed to remove excess dye. After air drying, colonies were photographed. This approach was used to assess the effects of CHE on 4T1 cell proliferation within a simulated tumor microenvironment.

DAPI staining for morphology assessment

4T1 cells and E0771 in the logarithmic growth phase were seeded into 6-well plates at a density of 2×10^5 cells/ml, with 2 ml per well. After 24 hours, the growth medium was replaced with CM and cultured for another 24 hours. Subsequently, the CM was aspirated, and cells were exposed to CHE at 6, 12, and 24 μM for 48 hours, while the control group received fresh medium. After treatment, cells were rinsed three times with PBS and fixed with 4 % paraformaldehyde for 10 min, followed by additional PBS washes. A 1 μg/ml DAPI solution was then applied, and cells were incubated at room temperature in the dark for 10–15 min to stain the nuclei. Excess dye was removed by PBS washing, and nuclear morphology was observed under a fluorescence microscope. Changes such as chromatin condensation and nuclear fragmentation were assessed based on DAPI fluorescence signals.

Mitochondrial membrane potential analysis

4T1 cells were cultured, grouped, and treated as outlined in Section 2.10.2. The mitochondrial membrane potential was evaluated using a JC-1 assay kit (120822230407, Shanghai Biyuntian Biotechnology Co., Ltd.) following the manufacturer's protocol and observed under a fluorescence microscope.

LDH release analysis

4T1 cells and E0771 cells were cultured, grouped, and treated as outlined in Section 2.10.2. Lactate dehydrogenase (LDH) release was quantified using the LDH Cytotoxicity Assay Kit (030016230506, Shanghai Biyuntian Biotechnology Co., Ltd.) following the manufacturer's protocol. Absorbance at 490 nm was recorded with a microplate reader to determine the extent of LDH release.

Evaluation of the effect of CHE on cell metastatic of BC pretreated with CM

Scratch wound healing assay

Cells were grown to confluence in 6-well plates, and a sterile 200 μl pipette tip was used to scratch the monolayer in a "#" pattern. After rinsing three times with PBS, initial images were captured using a light microscope. The cells were then pre-cultured in CM for 24 hours, followed by treatment with CHE at concentrations of 6, 12, and 24 μM. Additional images were taken at 24, 48, and 72 hours. Cell migration was quantified using ImageJ by measuring scratch widths, and the percentage of wound closure was calculated to evaluate the inhibitory effects of CHE.

Transwell chamber assay

4T1 cells and E0771cells were pre-cultured in CM for 24 hours and subsequently treated with CHE (6, 12, and 24 μM) for 48 hours to evaluate its impact on cell invasiveness under inflammatory conditions. In parallel, Matrigel was thawed overnight at 4 °C, diluted with RPMI 1640, and applied to Transwell inserts. After solidification for 6 hours, the inserts were prepared to mimic the extracellular matrix. Treated cells were then seeded into the Matrigel-coated inserts, with RPMI 1640 containing 10 % FBS added to the lower chamber as a chemoattractant. Following a 24-hour incubation, cells on the upper surface of the inserts were removed, while invasive cells were fixed, stained with crystal violet, and imaged. The number of invading cells was quantified using ImageJ to determine the effects of CHE on the invasive potential of cells.

Network pharmacology and transcriptomic analysis

Network pharmacology and omics data collection

CHE targets were identified and predicted through a network pharmacology-based approach utilizing the Traditional Chinese Medicine Systems Pharmacology Database (TCMSP) (Ru et al., 2014) and the PharmMapper database (He et al. 2024). Gene names were standardized and converted according to the UniProt database (UniProt Consortium, 2023). Single-cell transcriptomic data for breast tissue were retrieved from the Gene Expression Omnibus (GEO) database (Barrett et al., 2013) under accession number GSE161529 (Pal et al., 2021). This dataset comprises 69 scRNA-seq profiles, representing 421,761 cells from 52 patients, spanning normal, preneoplastic, and tumorigenic states. For this study, we selected a subset of 14 healthy breast tissue samples and 14 breast cancer (BC) tissue samples. The BC samples represent the major clinical subtypes, including 5 triple-negative breast cancer (TNBC) cases, 4 estrogen receptor-positive (ER+) cases, 4 human epidermal growth factor receptor 2-positive (HER2+) cases, and 1 progesterone receptor-positive (PR+) case.

Single cell differential gene expression analysis

Single-cell transcriptomic data from healthy and breast cancer (BC) tissues were analyzed using the Seurat package in R. Quality control measures excluded low-quality cells, which were defined as those with fewer than 200 detected genes, >10 % mitochondrial gene expression, or potential doublet contamination (Hao et al., 2024). The data were normalized using the "LogNormalize" method, and batch effects were addressed using the reciprocal principal component analysis (RPCA) method. Following normalization, dimensionality reduction was performed using principal component analysis (PCA), and cellular populations were visualized with t-distributed stochastic neighbor embedding (t-SNE) or uniform manifold approximation and projection (UMAP). Cell subpopulations were identified using a graph-based clustering algorithm, and cell types were annotated using the SingleR package (Aran et al., 2019) in conjunction with the CellMarker2 database (Hu et al., 2023). Samples were stratified into cancer and healthy cohorts, and pseudo-bulk data were generated by aggregating expression profiles of identical cell types across groups. Differential gene expression analysis was performed using the Seurat FindMarkers function, with statistical testing conducted via the DESeq2 package. DESeq2 model gene expression counts using a negative binomial distribution and applies the Benjamini-Hochberg procedure to control the false discovery rate. Differentially expressed genes (DEGs) were identified using an adjusted p-value threshold of 0.05 and an absolute log2 fold change ($|\log2FC| > 1$, criteria widely adopted in single-cell transcriptomics to ensure the robustness and biological relevance of results. Differentially expressed genes between groups within the same cell type were intersected with CHE target data to identify potential targets through which CHE may influence this cell type in the tumor microenvironment.

Bulk transcriptomic analysis

In this study, differential expression analysis of publicly available RNA sequencing data related to breast cancer (BC) was performed using the GEPIA2 N platform, an online tool based on TCGA and GTEx datasets. GEPIA2 enables the comparison of gene expression between BC and normal tissues (Tang et al., 2019). The "Differential Genes" function within the "Expression Analysis" module was employed to analyze the datasets. Significantly differentially expressed genes were identified using the Analysis of Variance (ANOVA) method. The identified genes were intersected with CHE targets in macrophages, which were previously identified through single-cell differential gene expression analysis, to derive the final set of CHE targets in the BC microenvironment. Additionally, the "General" section of GEPIA2 was applied for quick gene searches and to examine their differential expression across various cancer types.

Molecular docking

Compound structure files were retrieved from the PubChem database (Kim, 2016). The ligand Chelidonine (PubChem CID: 197810) was converted from SDF to PDB format using Open Babel 2.3.2 and further prepared in AutoDockTools by adding hydrogen atoms, assigning partial charges, detecting rotatable bonds, and exporting to PDBQT format. Receptor protein structures were obtained from the Protein Data Bank (PDB) database. The receptors used in this study were 7CVH (Human Fructose-1,6-bisphosphatase 1 in complex with geranylgeranyl diphosphate) and 3A29 (Crystal structure of human liver FBPase in complex with a tricyclic inhibitor). Receptor preprocessing involved removing water molecules, metal ions, and ligands using PyMOL 2.3.4 ("remove organic" command). Hydrogen atoms and partial charges were added using AutoDockTools, and the receptors were saved in PDBQT format. The active binding sites of the receptors were identified based on the positions of their co-crystallized ligands. Using PyMOL, the binding site coordinates were determined by selecting the known ligand and calculating the center of mass with the command "print (cmd.centerofmass ("sele"))". The grid box for docking simulations was configured using the following parameters: size_x = 22.5, size_y = 22.5, size_z = 22.5. Molecular docking simulations were performed using AutoDock Vina 1.1.2 (Eberhardt et al., 2021). The vina –config.txt command was used to execute the docking process. Docking results were analyzed using the Protein-Ligand Interaction Profiler (PLIP) (Schake et al.) to evaluate interactions, and the docking poses were visualized using PyMOL.

ELISA assay

The concentrations of interleukin 1β (IL-1β) and interleukin 6 (IL-6) in supernatants and homogenates were determined using ELISA kits (Wuhan Abebio Science Co., Ltd.) following the manufacturer's protocol. Supernatants, collected by centrifugation at 3000 × *g* for 10 min and stored at −20 °C, were thawed and diluted prior to analysis. Absorbance at 450 nm was measured with a microplate reader to complete the assay.

Western blotting assay

Tissues and cells were lysed in a lysis buffer containing PMSF (1:99, G2008, Servicebio) and incubated on ice for 15 min. The lysates were centrifuged at 12,000 rpm for 15 min at 4 °C, and the supernatants were collected. Total protein content was measured using a BCA protein assay kit (P0009, Beyotime) for quantification and normalization. Equal amounts of protein (20 μg) were resolved on 8−15 % SDS-PAGE gels and transferred to nitrocellulose (NC) membranes (FFN08, Beyotime).

The membranes were trimmed according to the molecular weights of the target proteins, blocked with 5 % skim milk at room temperature for 2 hours, and incubated overnight at 4 °C with specific primary antibodies, including CD206 (A8301, ABclonal.), Arg-1 9 (A1847, ABolonal), CD11c (WL05177, Wanleibio), NLRP3 (WL02635, Wanleibio), GSDMD (ab219800, abcam), GSDMDN (A20197, ABclonal), IL-18 (A23076, ABclonal), Caspase-1 (AF5418, Affinity Biosciences), Cleaved-Caspase 1 (AF4005, Affinity Biosciences), E-cadherin (WL01482, Wanleibio), N-cadherin (WL01047, Wanleibio), UEGFA (WL00009b, Wanleibio), MMP2 (WL03224, Wanleibio), Snail (A11794, ABclonal), Slug (A1057, ABclonal), FBP1 (YP-Ab-18296, UpingBio). STAT3 (bsm-52235R, Bioss antibodies), p-STAT3 (bs-1658R, Bioss antibodies), IL-6 (WL02841, Wanleibio), IL-1β (WL02257, Wanleibio), GAPDH (A19056, ABclonal), β-actin (AC026, ABclonal), α-tubulin (A6830, ABclonal), β-tubulin (YP-Ab-02968, UpingBio). After a 2-hour incubation with secondary antibodies at room temperature, immunoreactive bands were visualized using a gel imaging system following detection with enhanced chemiluminescence (ECL, P0018M, Beyotime).

Cell transfection

The day before transfection, RAW 264.7 cells were seeded in 6-well plates and incubated overnight to ensure the cell confluency reached approximately 70 % on the day of transfection. The siFBP1 (8470, GenePharma) powder was dissolved in nuclease-free water to a final concentration of 10 μM. For each well, 42.5 μl of buffer was added to a sterile nuclease-free EP tube, followed by 75 pmol of siFBP1. The mixture was pipetted up and down to ensure thorough mixing. Then, 15 μl of Plus transfection reagent was added to the siFBP1 premix, and the mixture was immediately pipetted several times to form siFBP1/Plus complexes. The prepared siFBP1/Plus complexes were added dropwise to the cells, followed by gentle manual shaking to ensure even distribution. The cells were then returned to the incubator and cultured under standard conditions (37 °C, 5 % CO_2) for further experiments as per the experimental design.

Reverse-transcription quantitative polymerase chain reaction (RT-qPCR)

Following the termination of cell culture, total RNA was isolated using Trizol reagent (Invitrogen, Carlsbad, CA, USA) in accordance with the manufacturer's instructions. The target gene primers were synthesized by Sangon Biotech (Shanghai, China), with the specific sequences as follows: Forward primer: GCATCGCACAGCTCTATGGT, Reverse primer: ACAGGTAGCGTAGGACGACT. For cDNA synthesis, 1 μg of RNA served as the template. Reverse transcription was carried out using the PrimeScript™ RT Master Mix (Perfect Real Time, RR037A, TaKaRa) under low-temperature conditions, strictly following the kit protocol. Quantitative PCR was performed using the TB Green™ Premix Ex Taq™ kit (RR420A) on a StepOnePlus™ Real-Time PCR System. The reaction mixture (15 μl) consisted of 7.5 μl of TB Green™ Premix, 0.3 μl of each 10 μM primer, 1 μl of cDNA template, and nuclease-free water to reach the final volume. PCR cycling conditions were set as: 95 °C for 30 s for initial denaturation, followed by 40 cycles of 95 °C for 5 s and 60 °C for 30 s for annealing/extension. Each sample was tested in triplicate for reliability, with β-actin used as the reference gene. The relative expression of mRNA was quantified using the 2-ΔΔCT method.

Statistical analysis

Statistical analyses were performed using GraphPad Prism 8. Results are expressed as the mean ± standard deviation (SD) from a minimum of three independent experiments. Comparisons at the same time point were analyzed using the independent samples *t*-test or one-way ANOVA. Post-hoc comparisons between groups were conducted with the LSD test. Statistical significance was set at $p < 0.05$, with $p < 0.01$ indicating high significance.

Results

CHE decelerates the growth of BC in vivo

To assess the potential of CHE in alleviating tumour growth *in vivo*, a breast cancer (BC) model was established by inoculating 4T1-luc cells into the axillary region of mice (Fig. 1B). Throughout the experiment, the body weight of mice in the control group remained stable and showed a gradual increase. In the Model group, the body weight of mice slightly increased in the early stages but then gradually decreased over time. After the administration of CHE in various groups, the body weight of mice showed a less pronounced decrease compared to the Model group. In contrast, treatment with CTX led to a pronounced weight loss in mice compared to the Model group (Fig. 1C). At the end of the treatment period, we assessed tumor size in the IVIS Lumina III system for imaging. The results illustrated that the Model group exhibited the highest tumor fluorescence signal intensity. In contrast, CHE treatment significantly decreased fluorescence signal intensity in a dose-dependent

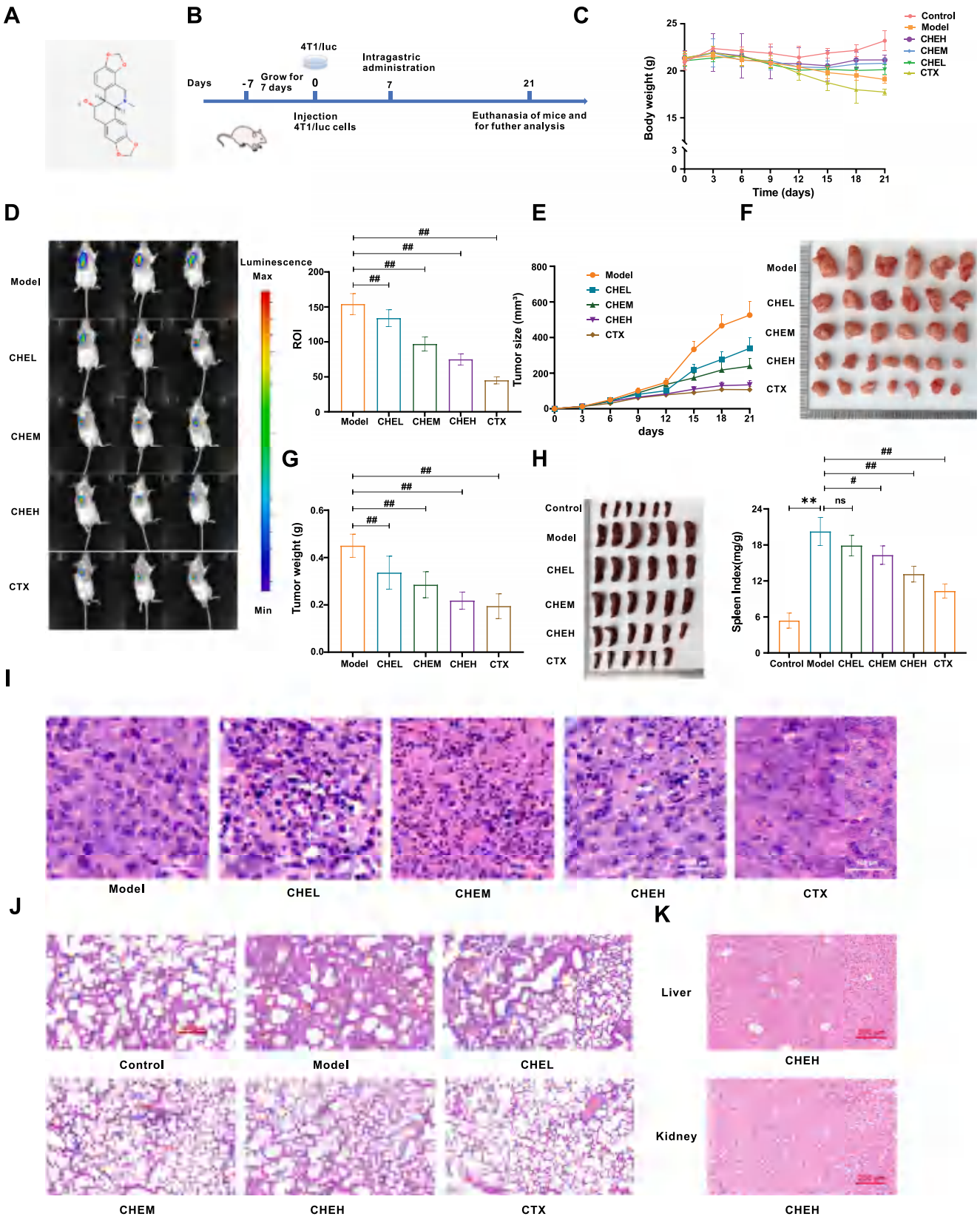

Fig. 1. CHE inhibits tumor growth in BC mice. (A) The chemical structure of CHE. (B) Schematic of the *in vivo* experimental protocol. (C) The weight of the mice ($n = 10$). (D) Bioluminescence imaging of tumor-bearing mice ($n = 3$). (E)Tumor volume changes ($n = 10$). (F) Tumor photo of mice. (G) Tumor weight ($n = 10$). (H) Spleen index ($n = 10$). (I) H&E staining of tumor tissues (40X, scale bar=100 μm, $n = 3$). (J) H&E staining of Lung tissues (20X, scale bar=200 μm, $n = 3$). (K) H&E staining of liver and kidney tissues (20X, scale bar=200 μm, $n = 3$). CHEL represents the low dose of chelidonine (5 mg/kg), CHEM represents the medium dose of chelidonine (10 mg/kg), CHEH represents the high dose of chelidonine (20 mg/kg), and CTX represents cyclophosphamide. $^{*}p < 0.05$, $^{**}p < 0.01$ vs. the control group; $\#p < 0.05$, $\#\#p < 0.01$ vs. the model group; ns, not significant.

manner. The CTX group exhibited an even greater reduction in fluorescence intensity compared to any of the CHE-treated groups ($p < 0.01$, Fig. 1D). Tumor volume was measured every three days, and a growth curve was generated. By day 15 after 4T1 cell inoculation, tumor volumes in the CHE-treated groups were significantly smaller than those in the Model group. The CTX group also demonstrated strong tumor growth suppression (Fig. 1E). The excised tumors showed that the Model group had the largest volume. CHE treatment reduced tumor size in a dose-dependent manner, while the CTX group exhibited the smallest tumors, consistent with the fluorescence signal intensity results (Fig. 1F). Tumor weight measurements further confirmed that CHE treatment significantly reduced tumor weight in a dose-dependent manner compared to the Model group. Notably, the CTX group displayed a more substantial reduction in tumor weight than any of the CHE-treated groups ($p < 0.01$, Fig. 1G). These findings indicate that CHE treatment effectively suppresses tumor growth in BC mice.

To investigate whether the tumor-suppressive effects of CHE are associated with immune modulation, the spleen index was evaluated across different groups. Compared to the Normal group, mice in the Model group exhibited significant spleen enlargement, suggesting that increased tumor burden may induce overactivation of the immune system. CHE treatment alleviated splenomegaly, suggesting that it may reduce immune overactivation or mitigate tumor-induced immune stimulation through immunomodulatory mechanisms. Similarly, the CTX group demonstrated a significant reduction in spleen index compared to the Model group. However, the spleen index in the CTX group was lower than that in the CHEH group, indicating a more pronounced effect of CTX in reducing splenomegaly ($p < 0.05$ or $p < 0.01$, Fig. 1H). In summary, CHE treatment may improve splenomegaly by reducing immune burden or modulating the immune response.

HE staining revealed clear pathological differences among the groups. In the Model group, tumor cells were densely packed, with intact nuclei and minimal signs of degeneration, indicating active tumor growth. In the CHEL group, mild pathological changes were observed, including slight nuclear shrinkage (pyknosis) and sporadic chromatin condensation. The CHEM group showed more evident features of nuclear degeneration, such as increased pyknosis and occasional nuclear fragmentation (karyorrhexis). The CHEH group exhibited the most pronounced pathological changes among the CHE-treated groups, including significant nuclear damage, cytoplasmic disintegration, and disrupted cell membranes, suggesting enhanced anti-tumor effects. The CTX group, in contrast, displayed widespread and uniform pathological changes, including extensive nuclear fragmentation, chromatin condensation, and cytoplasmic damage. Overall, CHE treatment induced dose-dependent tumor cell damage, particularly at higher doses (Fig. 1I).

The analysis of lung metastasis among the different treatment groups revealed distinct pathological features. In the Control group, which was not inoculated with tumor cells, the lung tissue displayed normal alveolar structures without any evidence of metastatic lesions. In the Model group, lung tissues exhibited extensive metastatic nodules, with dense clusters of tumor cells infiltrating the alveolar spaces, indicating significant tumor burden. Treatment with CHE demonstrated dose-dependent reductions in lung metastases. In the CHEL group, the metastatic burden was moderately reduced, with fewer and smaller tumor nodules compared to the Model group. The CHEM group showed further reductions in tumor infiltration, with clearer alveolar structures and smaller metastatic lesions. Notably, the CHEH group exhibited the most marked improvement among the CHE-treated groups, with minimal tumor cell infiltration and nearly normal lung morphology, suggesting strong anti-metastatic effects at higher doses. The CTX group also demonstrated significant anti-metastatic effects, with a reduction in metastatic nodules and preservation of alveolar structures. However, the lung morphology in the CTX group showed slightly more residual damage compared to the CHEH group, possibly due to the higher toxicity of CTX. In summary, CHE treatment effectively reduced lung metastases in a dose-dependent manner, with the CHEH group achieving results comparable to those of CTX, but with potentially lower toxicity (Fig. 1J).

The HE staining of liver and kidney tissues in the CHEH group was analyzed to evaluate potential toxicity at high CHE doses. Liver tissues in the CHEH group displayed well-preserved lobular architecture, with distinct hepatic cords and intact central veins. No signs of hepatocyte necrosis, inflammatory infiltration, or structural abnormalities were observed, indicating an absence of hepatotoxicity. Similarly, kidney tissues showed well-preserved glomerular and tubular structures without evidence of glomerular atrophy, tubular necrosis, or inflammatory cell infiltration, suggesting no nephrotoxicity (Fig. 1K).

Overall, the results of these *in vivo* experiments indicate that CHE can alleviate tumour growth in BC mice and inhibit metastasis, with the CHEH group showing particularly remarkable efficacy. The mechanism of action is likely mediated by a combination of direct anti-tumor effects and immune system modulation, underscoring the potential of CHE as a promising therapeutic agent for BC treatment. To further investigate these findings, we aimed to elucidate the underlying mechanisms of CHE's anti-tumor activity, with a particular focus on its immunomodulatory effects within the tumor immune microenvironment (TME). Given that tumor-associated macrophages (TAMs) predominantly adopt a pro-tumoral M2 phenotype, which promotes immune suppression and tumour progression, we hypothesized that CHE may exert its effects by regulating macrophage polarization.

CHE suppresses M2 macrophage polarization

The experimental results showed that CD206 fluorescence expression was strongly detected in tumor tissues of the model group, indicating significant polarization of M2 macrophages. After CHE treatment, the number of CD206-positive cells was notably reduced, suggesting that M2 macrophage polarization was inhibited. Following CTX treatment, CD206 fluorescence signals were further diminished. In contrast, CD86 expression in the model group was relatively weak, indicating a lower presence of M1 macrophages. After CHE administration, no significant changes in CD86 expression were observed at low and medium doses, while its fluorescence expression significantly increased at high doses. CTX treatment also resulted in a marked increase in CD86 expression. These findings suggest that CHE has the potential to regulate macrophage polarization. ($P<0.01$, Fig. 2A).

Furthermore, Western blot analysis was employed to examine the expression of polarization marker proteins in the tumor tissues of BC model mice. The study disclosed that in the Model group, CD206 and Arg-1 proteins were highly expressed, while CD86 expression was low. However, following CHE administration, the expression levels of CD206 and Arg-1 significantly decreased, while the expression level of CD86 increased significantly. After CTX administration, protein expression levels exhibited a similar trend to those observed with CHE treatment but were more pronounced. ($p < 0.05$ or $p < 0.01$, Fig. 2B). This indicates that CHE has the ability to inhibit M2 macrophage polarization and promote M1 macrophage polarization *in vivo*, with a more consistent effect on suppressing M2 polarization.

To further investigate the impact of CHE on M2 macrophages, we initiated the experiment by inducing the differentiation of RAW264.7 cells into M2 macrophages. IL-4 was employed as the inducer for the differentiation process. As the concentration of IL-4 increased, the RAW264.7 cells underwent morphological changes, transforming from a rounded shape to elongated spindle-like or irregular polygonal forms, accompanied by enhanced pseudopodia extension and stronger adhesion to the culture dish. Similar morphological alterations were noted at IL-4 concentrations of 20 ng/ml and 40 ng/ml (Figure S1A).

Fluorescence microscopy was subsequently employed to examine the expression of the M2 macrophage polarization marker, CD206. The results revealed a significant, dose-dependent increase in CD206 fluorescence intensity following IL-4 stimulation, compared to unstimulated

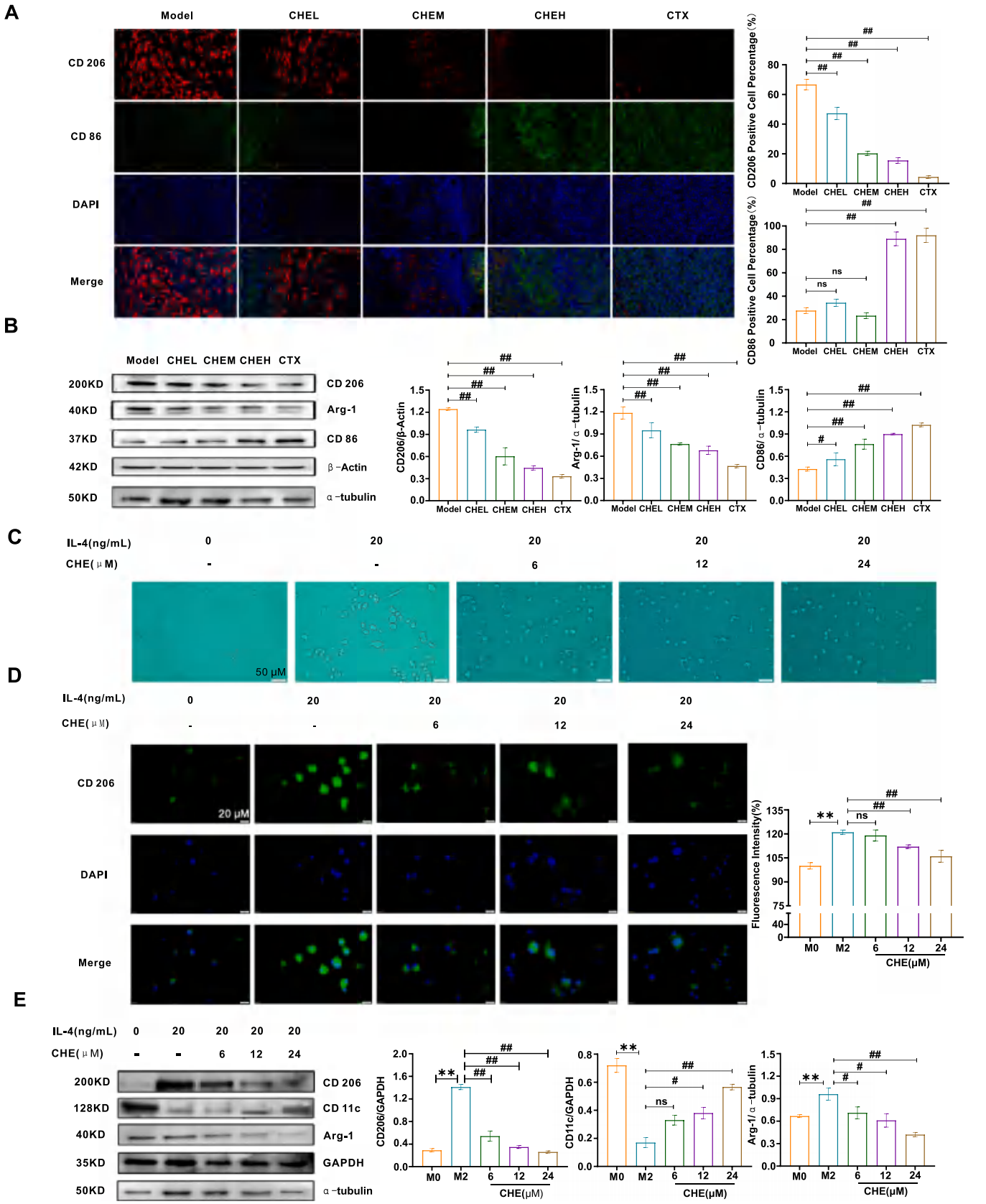

Fig. 2. CHE inhibits M2 macrophage polarization. (A) The fluorescent expressions of CD206 and CD86 in BC mice tumor tissue ($n = 3$). (B) Western blot analysis of the relative expression levels of CD206, CD86, and Arg-1 proteins in tumor tissues of mice ($n = 3$). (C) Impact of CHE on macrophage morphology (20 ×, scale bar: 50 μm, $n = 3$). (D) Influence of CHE on CD206 fluorescence intensity in macrophages (40 ×, scale bar: 20 μm $n = 3$). (E) Western blot analysis of the relative expression levels of CD206, CD11c and Arg-1 proteins in RAW264.7 cells ($n = 3$). *$p < 0.05$, **$p < 0.01$ vs. the M0 group; #$p < 0.05$, ##$p < 0.01$ vs. the M2 group or the model group; ns, not significant.

cells. However, no notable difference in fluorescence intensity was observed between the 20 ng/ml and 40 ng/ml IL-4 treatment groups. IL-4 treatment groups, indicating that IL-4 reached a saturation point at 20 ng/ml ($p < 0.01$, Figure S1B). These findings verified that IL-4 could effectively induce the polarization of RAW264.7 cells towards the M2 phenotype, and thus a concentration of 20 ng/ml IL-4 was selected for subsequent experiments.

Western blot analysis further confirmed these findings, showing that IL-4 stimulation significantly upregulated the protein expression levels of M2 polarization markers CD206 and Arg-1 compared to unstimulated M0 macrophages. These results validate that 20 ng/ml of IL-4 effectively induces the differentiation of RAW264.7 cells into M2 macrophages ($p <$ 0.01, Figure S1C).

To determine the optimal dosage of CHE for RAW264.7 cells, a CCK-8 assay was performed to evaluate cell viability following 48 hours of CHE treatment. The results showed that CHE had no significant effect on RAW264.7 cell proliferation at concentrations ranging from 0 to 40 μM ($p > 0.05$, Figure S2). Previous studies have reported that CHE inhibits cancer cell proliferation at doses of 6–30 μM while exhibiting minimal cytotoxicity toward RAW264.7 cells. Based on these findings, CHE concentrations of 6, 12, and 24 μM were selected for subsequent experiments. To investigate the effects of CHE on M2 macrophages, RAW264.7 cells were first induced to differentiate into M2 macrophages using 20 ng/ml IL-4, followed by treatment with CHE at the selected concentrations.

Optical microscopy observations revealed that upon IL-4 induction, RAW264.7 cells transformed from an oval shape to an adherent morphology, assuming an elongated spindle shape or irregular polygonal form with pseudopodia. As the concentration of CHE increased, the formation of pseudopodia gradually diminished. At higher CHE doses, a significant number of cells reverted to an oval shape reminiscent of uninduced cells. These findings suggest that CHE inhibits M2 macrophage polarization in a dose-dependent manner (Fig. 2C).

Fluorescence microscopy was then utilized to observe the fluorescence expression of the M2 polarization marker protein, CD206, after CHE treatment. The results showed that IL-4 induction led to a substantial increase in the fluorescence intensity of CD206. While treatment with 12 μM and 24 μM of CHE significantly attenuated this effect, indicating that CHE is capable of inhibiting M2 macrophage polarization ($p < 0.01$, Fig. 2D).

Western blot analysis provided further evidence supporting these observations. IL-4 stimulation notably increased the expression of M2 markers CD206 and Arg-1 while suppressing the M1 marker CD11c in RAW264.7 cells. In contrast, CHE treatment (6–24 μM) reversed this trend by significantly reducing CD206 and Arg-1 levels and upregulating CD11c expression. These findings indicate that CHE may regulate macrophage polarization by shifting the balance from the M2 phenotype toward the M1 phenotype ($p < 0.05$ or $p < 0.01$, Fig. 2E).

These findings indicate that CHE effectively suppresses M2 macrophage polarization in both *in vivo* and *in vitro* settings. This regulatory effect on macrophage polarization may represent a key mechanism by which CHE inhibits tumor progression in BC model mice.

CHE inhibits BC proliferation within TME via pyroptosis induction

Tumor cell proliferation was assessed via Ki67 immunohistochemical staining. The results revealed a significantly higher proportion of Ki67-positive cells in the Model group, indicating elevated tumor cell proliferation. In contrast, CHE treatment groups (CHEL, CHEM, CHEH) exhibited a dose-dependent reduction in Ki67-positive cell proportions. Similarly, the CTX group demonstrated a notable decrease in Ki67-positive cells, comparable to the CHEH group. These results highlight the potent inhibitory effect of CHE on tumor cell proliferation ($p < 0.05$ or $p < 0.01$, Fig. 3A).

To further explore whether the anti-proliferative effects of CHE are linked to pyroptosis, Western blot analysis was conducted on mouse tumor tissues. Compared to the Model group, CHE treatment significantly increased the expression of NLRP3, GSDMD, GSDMD-N, Caspase-1, c-Caspase-1, and IL-18. A similar trend was observed in the CTX group ($p < 0.05$ or $p < 0.01$, Fig. 3B). These findings suggest that CHE may

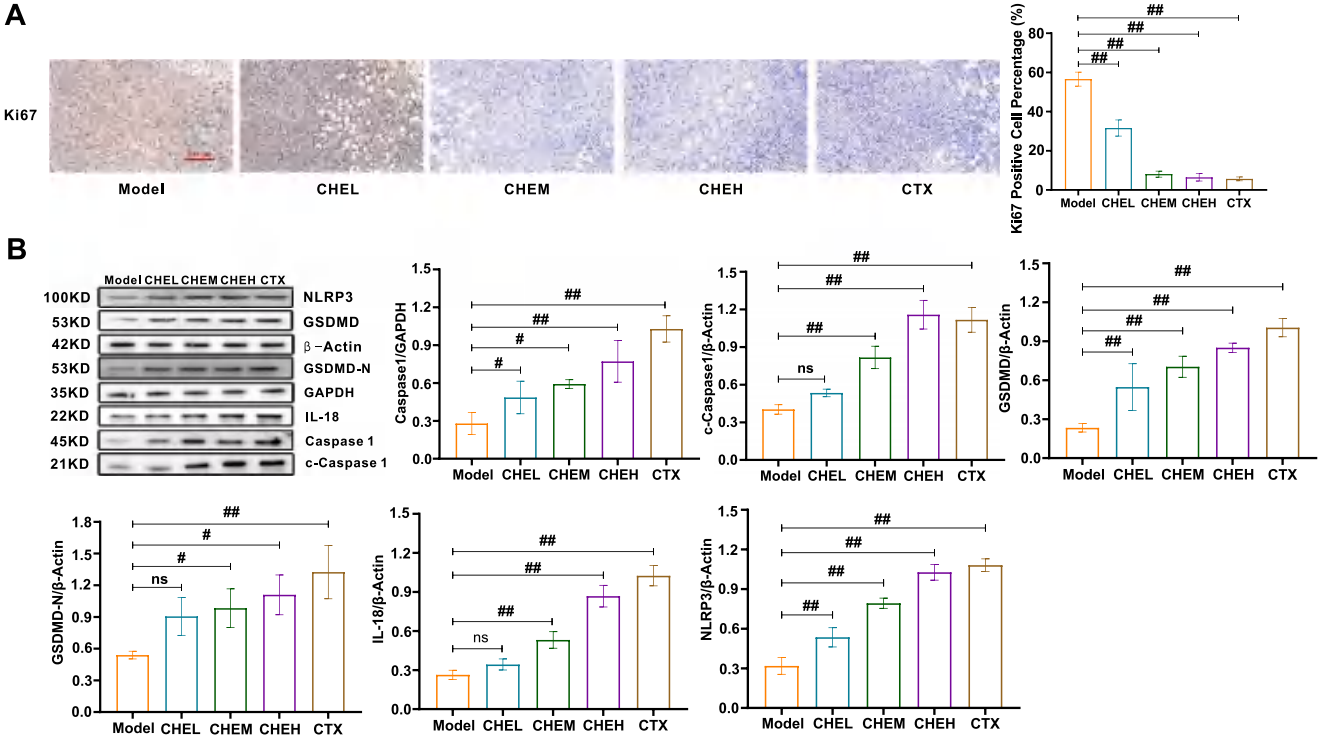

Fig. 3. The mechanism of CHE's anti-tumor proliferative effect *in vivo*. (A) Expression of Ki67 in Tumor Tissues ($n = 3$). (B) Expression of pyroptosis-related proteins in BC tissues ($n = 3$).

inhibit tumor proliferation by triggering pyroptosis, likely via activation of the NLRP3/Caspase-1/GSDMD signaling pathway.

To investigate whether the anti-tumor effects of CHE are related to the suppression of macrophage M2 polarization, a co-culture system of RAW264.7 and 4T1 cells was established. Using a CCK-8 assay, the proliferation of 4T1 cells treated with conditioned media (CM) was assessed under different CHE concentrations. The half-maximal inhibitory concentration (IC_{50}) values were determined to be 18 μM for the Control group, 20 μM for the M0-CM group, and 51 μM for the M2-CM group. These findings reveal that CM treatment reduces the sensitivity of 4T1 cells to CHE, with the M2-CM group exhibiting the weakest inhibitory response to CHE-induced suppression of proliferation. Based on these findings, CHE concentrations ranging from 6 μM to 24 μM were selected for subsequent experiments (Fig. 4A). The same experiment was conducted using another breast cancer cell line, E0771, and the results exhibited a similar trend (Figure S3A).

A single-cell colony formation assay was conducted to examine the growth potential of 4T1 cells under different experimental conditions. The results revealed that, in comparison to the M0-CM group, 4T1 cells treated with M2-CM formed significantly more and larger colonies. When compared to the M2-CM group, CHE treatment (6–24 μM) markedly and dose-dependently reduced the number and size of 4T1 cell colonies, indicating that M2-CM can promote 4T1 cell proliferation, which can be effectively inhibited by CHE ($p < 0.05$ or $p < 0.01$, Fig. 4B).

DAPI staining was used to observe changes in nuclear morphology of 4T1 cells under different conditions. The results showed that, compared with the M2-CM group, 4T1 cells treated with CHE (6–24 μM) exhibited a significant reduction in nuclear number, weakened blue fluorescence, chromatin condensation, and nuclear fragmentation. These findings suggest that CHE might influence tumor cell survival in the tumor microenvironment by inducing apoptosis or inhibiting cell proliferation (Fig. 4C). A similar experiment was conducted using E0771 cells, where CHE treatment also resulted in a reduction in nuclear number and the occurrence of nuclear fragmentation (Figure S3B).

To investigate whether the anti-proliferative effect of CHE on 4T1 cells treated with M2-CM is related to alterations in mitochondrial membrane potential, JC-1 staining was utilized to assess mitochondrial function in 4T1 cells under diverse conditions. The study found that, compared to the Control group, no significant change was observed in the ratio of JC-1 aggregates to monomers in the M0-CM and M2-CM groups ($p > 0.05$). However, after CHE treatment (6–24 μM), the ratio showed no considerable change in the low-dose group, while it significantly decreased in the high-dose group ($p < 0.05$), This suggests that the anti-tumor effect of CHE might be linked to the induction of mitochondrial apoptosis (Fig. 4D).

An LDH release assay was conducted to evaluate the effect of CHE on cell membrane integrity in 4T1 cells treated with M2-CM. The results showed a decreased LDH release in the M2-CM group compared to the M0-CM group. Conversely, CHE significantly enhanced LDH release in 4T1 cells treated with M2-CM, indicating that CHE disrupted cell membrane integrity and affected cell function. This process might be related to pyroptosis ($p < 0.05$ or $p < 0.01$, Fig. 4E). The same trend in results was also observed in E0771 cells (Figure S3C).

To further confirm that the suppression of 4T1 cell proliferation by CHE in M2-CM-treated cells is associated with pyroptosis, Western blot analysis was carried out to examine the expression of pyroptosis-related proteins, including NLRP3, GSDMD, GSDMD-N, Caspase-1, c-Caspase-1, and IL-18, under different treatment conditions. Compared with the M2-CM group, CHE treatment (6–24 μM) significantly upregulated the expression of GSDMD, GSDMD-N, IL-18, NLRP3, and c-Caspase-1 ($p < 0.01$, Fig. 4F). This indicates that the anti-proliferative effect of CHE on M2-CM-treated 4T1 cells is associated with pyroptosis and might be mediated by the activation of the NLRP3/Caspase-1/GSDMD pathway, thereby triggering pyroptosis in 4T1 cells. To further investigate the mechanism by which CHE inhibits pyroptosis in 4T1 cells, the NLRP3 inhibitor MCC950 (10 μM, HY-12815, MCE) was used to determine whether blocking pyroptosis could negate the effects of CHE. The results showed that high-dose CHE treatment significantly increased the expression of GSDMD, GSDMD-N, IL-18, NLRP3, and c-Caspase-1. However, this upregulation was markedly suppressed when combined with MCC950 treatment ($p < 0.05$ or $p < 0.01$, Fig. 4G).

In summary, this study uncovers that CHE induces pyroptosis in BC cells by regulating mitochondrial membrane potential, disrupting cell membrane integrity, and activating the NLRP3/Caspase-1/GSDMD pathway.

CHE inhibits BC metastasis within TME via EMT suppression

CHE was found to significantly inhibit breast cancer metastasis, as evidenced by the analysis of lung tissue pathological sections. To further explore its effects on the migration and invasion capabilities of breast cancer cells, we performed scratch assays, Transwell assays, and analyzed the expression of EMT-related proteins. In the wound-healing assay, compared with the M0-CM group, the M2-CM group markedly enhanced the migration ability of 4T1 cells at both 48 and 72 hours. However, CHE (6–24 μM) treatment significantly inhibited the M2-CM-induced migration of 4T1 cells ($p < 0.01$, Fig. 5A). Meanwhile, the Transwell invasion assay revealed that M2-CM significantly enhanced the invasive capacity of 4T1 cells. However, treatment with CHE (6–24 μM) significantly reduced this M2-CM-induced invasiveness ($p < 0.01$, Fig. 5B). We also performed Transwell assays using E0771 cells to evaluate the inhibitory effect of CHE on the invasive capabilities of breast cancer cells. The results showed that M2-CM significantly enhanced the invasive ability of E0771 cells, while CHE (6–24 μM) markedly suppressed the M2-CM-induced invasion of E0771 cells ($p < 0.01$, Figure S3D).

Immunohistochemical analysis of CD31 expression in tumor tissues revealed abundant CD31-positive cells in the model group, indicating a high level of angiogenesis. However, treatment with different doses of CHE resulted in a dose-dependent reduction in CD31 expression. The CHEH group demonstrated a significant reduction in CD31-positive cells compared to the model group, with the CTX group exhibiting the strongest suppression of CD31 expression ($p < 0.01$, Fig. 5C). These findings suggest that CHE effectively suppresses angiogenesis in tumor tissues.

Western blot analysis was conducted to determine whether the inhibitory effects of CHE on migration and invasion are linked to epithelial-mesenchymal transition (EMT). M2-CM treatment was found to upregulate mesenchymal markers, including N-Cadherin, Snail, Slug, MMP2, and VEGFA, while significantly reducing the expression of the epithelial marker E-Cadherin in 4T1 cells. CHE treatment, particularly at 12–24 μM, reversed these effects by significantly increasing E-Cadherin levels and reducing N-Cadherin, Snail, Slug, MMP2, and VEGFA expression. These results indicate that CHE inhibits migration and invasion through its regulation of EMT ($p < 0.01$, Fig. 5D).

To confirm whether the inhibitory effect of CHE on EMT extends to an *in vivo* setting, Western blot analysis was performed on lung tissue from BC-bearing mice. The model group, compared to normal mice, exhibited significant upregulation of mesenchymal markers (N-Cadherin, Snail, Slug, MMP2, and VEGFA) and downregulation of the epithelial marker E-Cadherin. CHE treatment reversed these changes, significantly increasing E-Cadherin expression while reducing N-Cadherin, Snail, Slug, MMP2, and VEGFA levels. Similar trends in protein expression were observed in the CTX group, consistent with those in the CHE-treated groups. These results suggest that CHE regulates EMT *in vivo* ($p < 0.05$ or $p < 0.01$, Fig. 5E).

Collectively, CHE effectively mitigates the EMT mitigate of process in BC both *in vitro* and *in vivo*, thereby inhibiting cancer cell migration, invasion, and subsequent crucial processes related to angiogenesis.

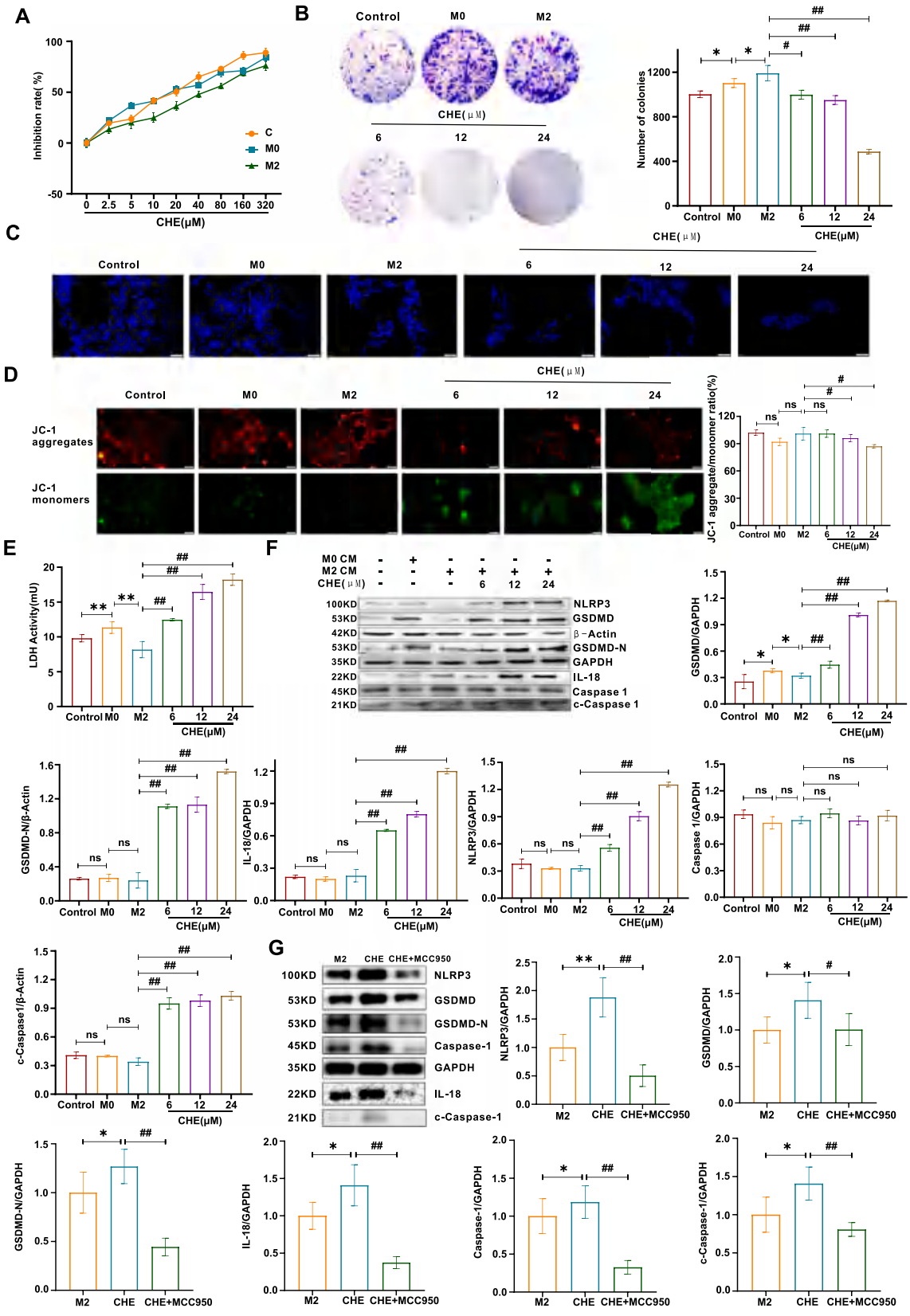

Fig. 4. Mechanism of CHE inhibiting BC cell proliferation in conditioned medium. (A) Inhibition proliferation of CHE on the CM-treated 4T1 cells ($n = 6$). (B) Impact on colony formation in CM-treated 4T1 cells ($n = 3$). (C) Effects on nuclear morphology of CM-treated 4T1 cells (scale bar: 50μ m, $n = 3$). (D) Influence on mitochondrial membrane potential in CM-treated 4T1 cells(scale bar: 50μ m $n = 3$). (E) Effect on LDH release from CM-treated 4T1 cells ($n = 6$). (F) Impact of CHE on pyroptosis-related protein expression in CM-treated 4T1 cells ($n = 3$). (G) Expression of pyroptosis-related proteins after MCC950 treatment ($n = 3$). B-F: $^{*}p < 0.05$, $^{**}p < 0.01$ vs. the M0 group; $\#p < 0.05$, $\#\#p < 0.01$ vs. the M2 group or the model group; ns, not significant. G: $^{*}p < 0.05$, $^{**}p < 0.01$ vs. the M2 group; $\#p < 0.05$, $\#\#p < 0.01$ vs. the CHE group.

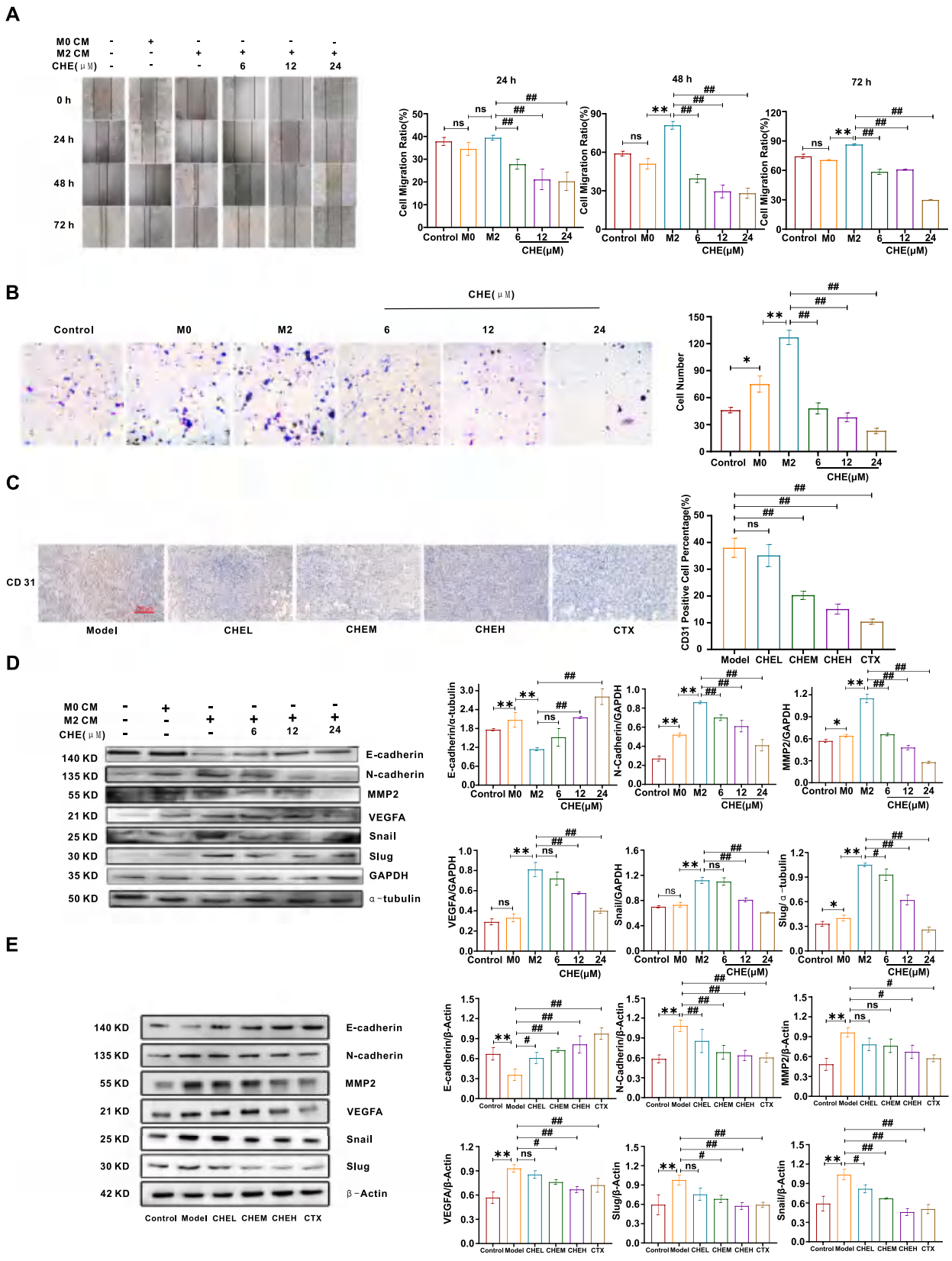

Fig. 5. The mechanism by which CHE inhibits BC metastasis. (A) Result of scratch assay ($n = 3$). (B) Result of transwell invasion assay ($n = 3$). (C) Expression of CD31 in Tumor Tissues ($n = 3$). (D, E) Expressions of EMT-related proteins by western blot ($n = 3$). $^{*}p < 0.05$, $^{**}p < 0.01$ vs. the M0 group or the control group; $\#p < 0.05$, $\#\#p < 0.01$ vs. the M2 group or the model group; ns, not significant.

FBP1 as a key target potentially through which CHE influencing M2 macrophage polarization

To investigate the potential targets by which CHE inhibits tumor growth through targeting M2 macrophages, we employed single-cell transcriptomics combined with network pharmacology approaches. First, network pharmacology using TCMSP and PharmMapper (Fit Score $\geq$ 0.8) yielded 258 high-confidence CHE targets. Second, using the single-cell transcriptomic data from the GSE161529 dataset (comprising 14 healthy tissues and 14 BCE tissue samples), we analyzed the cellular composition and differentially expressed genes associated with BC. Through the application of batch effect correction techniques and cell clustering algorithms, we successfully identified 12 distinct cell clusters (Fig. 6A). Based on well-established marker genes and the use of automated software for annotation, these 12 clusters were further categorized into 8 different cell types (Fig. 6B), including epithelial cells (clusters 0 and 1), B cells (clusters 2, 11, and 12), fibroblasts (clusters 3, 4, and 10), exhausted CD8+ T cells (cluster 5), endothelial cells (cluster 6), macrophages (cluster 7), T cells (cluster 8), and tissue stem cells (cluster 9). Cell type classification was determined by specific marker genes, such as CD79A for B cells, PDGFRB for fibroblasts, KLRD1 for exhausted CD8+ T cells, PECAM1 for endothelial cells, and CD68 for macrophages, while other cell types were annotated using SingleR (Fig. 6C). Comparative analysis of cellular distributions between cancerous and normal tissues revealed a notable increase in the populations of immune cells within cancer tissues (Fig. 6D).

Further clustering analyses of macrophages in cluster 7 identified various macrophage subtypes, including M1 macrophages (Mph (like_M1)_03_IL6), M2 macrophages (Mph(M2)_02_PPARG, Mph (like_M2)_07_TGFB3), monocytes (Mono-like_06_CD14), and intermediate-state macrophages (Mph(mix)_01_ FAM167B, Mph(mix) _04_RUNX1T1, Mph(mix)_05_TOX3, Mph(mix)_08_SIX1) (Fig. 7E). M2 macrophages are markedly more prevalent in cancer tissues compared to normal tissues ($p < 0.001$, Fig. 6F). To explore the potential impact of CHE on M2 macrophage polarization, we performed differential expression analysis of M2 macrophages between cancerous and normal tissues, applying stringent selection criteria ($p < 0.05$, $|\log2FC|>1$). The intersection of the 258 targets identified through network pharmacology for CHE with differentially expressed genes in M2 macrophages resulted in 11 significant targets, including MTF1, GALM, CLIC4, RBM22, GTF2B, CUL5, FBP1, DICER1, SNX9, EP300, and TPR (Fig. 6G).

Bulk differential gene expression analysis was carried out between normal breast tissue and BC tissue by using the GEPIA2 platform. Stringent criteria were applied to identify significantly differentially expressed genes, with $|\log2\ FC| > 1$ and adjusted P-value < 0.01. A total of 3356 differentially expressed genes were identified, and their chromosomal distribution was illustrated in Figure S4A. Genes with decreased expression in cancer tissue relative to normal tissue are marked in green, while those with increased expression were marked in red. To explore potential therapeutic targets, the 3356 differentially expressed genes were intersected with genes associated with CHE, which were identified through network pharmacology, yielding a list of 12 potential targets (Fig. 7A), namely CCND1, MYO6, VAV3, SPC25, FBP1, ACTA1, ALDH18A1, MB, F10, PTGS2, ADRB2, and CCNB1. These 12 targets were then further intersected with the 11 potential targets identified through single-cell transcriptomic analysis, leading to the identification of FBP1 as the only overlapping gene (Fig. 7B). The integration of bulk and single-cell analyses offers key advantages. Bulk analysis provides a comprehensive overview of global gene expression changes, capturing the overall molecular landscape of tissues. Meanwhile, single-cell analysis enables the identification of cell-type-specific changes, ensuring the selected targets are not only differentially expressed but also relevant to specific cell populations. The overlap of FBP1 in these two independent analyses highlights its robustness as a candidate.

FBP1, a key enzyme in glycolysis and gluconeogenesis, plays an important role in regulating macrophage metabolic states, potentially affecting their polarization. Single-cell transcriptomic analysis revealed higher FBP1 expression in cancer tissues compared to normal tissues, consistent with results from bulk data analysis (Fig. 7C and Figure S4B).

To further validate the interaction between CHE and its primary target FBP1, molecular docking analysis was conducted using the PDB structures 3A29 and 7CVH (Fig. 7D). Docking simulations were performed three times to ensure reproducibility, and the mean binding energies, standard deviations, and predicted pKi values were calculated. For PDB 3A29, the docking was centered at (7.57, 60.46, 32.09). The binding energies were −7.893, −7.892, and −7.889 kcal/mol, with a mean binding energy of −7.89±0.002 kcal/mol. The predicted pKi value for CHE was 1.36 μM. CHE primarily interacted with FBP1 through hydrophobic interactions (e.g., ALA24 and LEU30) and hydrogen bonds (e.g., LEU30, THR31, and TYR113) (Table S1, S2). For PDB 7CVH, the docking was centered at (−4.40, −22.19, −47.42). The binding energies were −7.065, −6.99, and −6.80 kcal/mol, with a mean binding energy of −6.95±0.11 kcal/mol. The predicted pKi values for CHE ranged from 2.1 to 3.3 μM, indicating moderate to strong binding affinity. Interaction analysis showed hydrophobic interactions with 245TYR and 265TYR, as well as hydrogen bonds with 123GLY, 124SER, 125SER, 213ASN, 265TYR, 275LYS, and 277ARG (Table S3, S4). Additionally, a π-cation interaction was observed with 275LYS, which likely enhanced the binding stability. Although CHE exhibited slightly weaker binding energy compared to the known ligand AMP analog 8 l (PDB 3A29, IC50 = 0.013 μM), it still demonstrated strong binding affinity, as binding energies below −7 kcal/mol are generally considered favorable. The known ligand 8 l achieved stronger binding through additional hydrogen bonds and water bridges, such as with GLY28 and GLU29.

In summary, FBP1 has been identified as a potential primary target that may influence M2 macrophage polarization. Its elevated expression in BC tissues, its strong binding affinity with CHE highlight its critical role in BC progression and its potential as a therapeutic target in the context of CHE-based therapies.

Suppression of CHE on macrophage M2 polarization relates to the inhibition of FBP1/STAT3 pathway

To further verify that FBP1 is the pivotal target through which CHE inhibits M2 macrophage polarization, we analyzed the expression levels of FBP1 in macrophages using Western blot. It was illustrated that, following IL-4 treatment, FBP1 protein expression was markedly upregulated. Conversely, after treatment with CHE (6–24 μM), the levels of FBP1 protein were notably reduced ($p < 0.01$, Fig. 8A).

STAT3 activation is strongly linked to M2 macrophage polarization. Western blot analysis showed that IL-4-induced polarization in RAW264.7 cells did not alter STAT3 expression ($p > 0.05$), but significantly increased p-STAT3 levels. Following CHE treatment, STAT3 expression remained unchanged ($p > 0.05$), whereas p-STAT3 levels were significantly reduced ($p < 0.01$, Fig. 8B).

IL-6 activates the STAT3 signaling pathway by promoting STAT3 phosphorylation. Chronic low levels of IL-1β can trigger the secretion of IL-6 and other factors, further amplifying STAT3 activation and driving M2 polarization. ELISA analysis of the cell supernatant showed that IL-4 treatment significantly decreased IL-1β levels while increasing IL-6 levels. In contrast, CHE treatment (6–24 μM) significantly reduced IL-6 levels while dose-dependently increasing IL-1β secretion ($p < 0.05$ or $p < 0.01$, Fig. 8C). Western blot analysis further confirmed these results: IL-4 markedly reduced IL-1β expression and upregulated IL-6, whereas CHE (6–24 μM) significantly lowered IL-6 levels and elevated IL-1β expression ($p < 0.01$, Fig. 8D).

To determine whether CHE influences the expression of IL-6, IL-1β, STAT3, and p-STAT3 proteins in tumor tissues *in vivo*, Western blot analysis was conducted. Compared to the Model group, CHE treatment reduced IL-6 expression while increasing IL-1β levels. STAT3 protein levels remained unchanged ($p > 0.05$), but p-STAT3 expression was

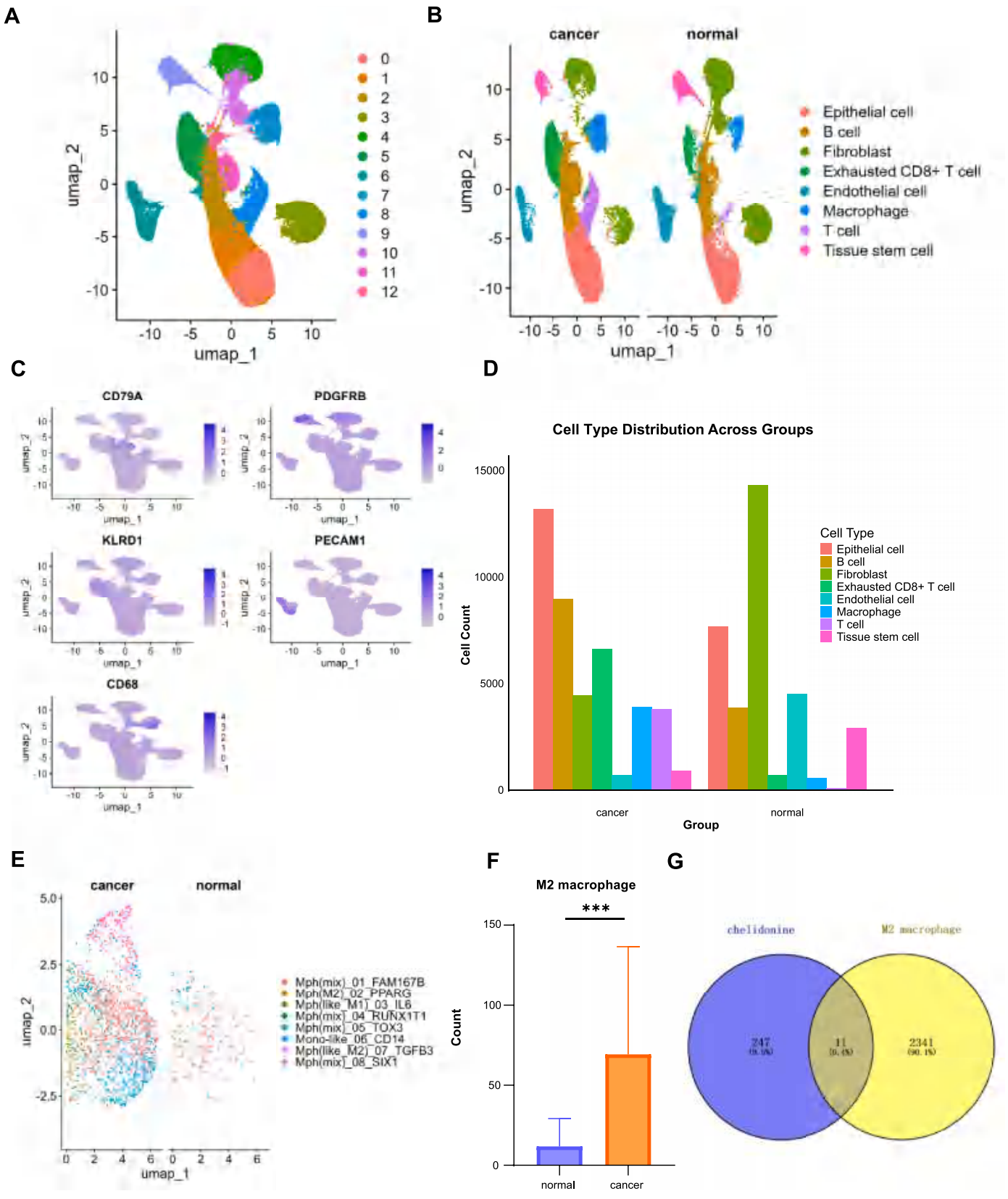

Fig. 6. Single-Cell transcriptomic analysis. (A) UMAP visualization of the initial clustering; (B) Cell type annotation; (C) Marker genes used for cell type annotation; (D) Distribution of different cell types between BC and normal tissues; (E) Subtypes of macrophages; (F) Distribution of M2 macrophages between groups ($n = 14$); (G) Venn diagram showing the intersection of CHE targets and differentially expressed genes in M2 macrophages. ***$p < 0.01$ vs. the normal group.

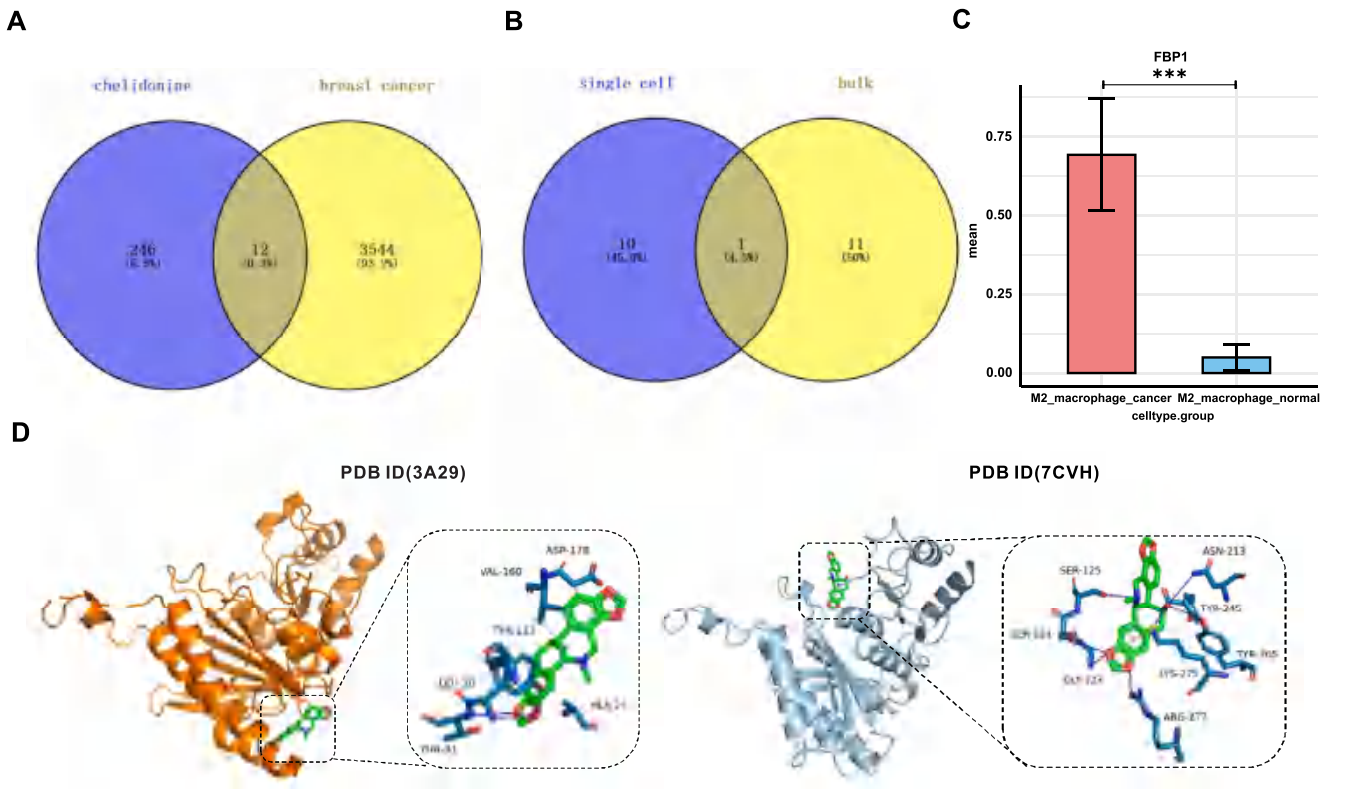

Fig. 7. Bulk RNA-seq analysis and molecular docking. (A) Venn diagram showing the overlap between DEGs from bulk RNA-seq analysis and the targets of CHE. (B) Venn diagram illustrating the intersection of CHE targets identified in single-cell RNA-seq analysis and those identified in bulk RNA-seq analysis. (C) Bar plot demonstrating the expression levels of FBP1 in M2 macrophages across experimental groups ($n = 14$). (D) Molecular docking visualization of the interaction between CHE and FBP1(PDB ID (3A29), PDB ID (7CVH)). ***$p < 0.01$ vs. the normal group.

significantly downregulated. The CTX group exhibited a protein expression trend similar to that of the CHE group. These findings were consistent with the *in vitro* result ($P<0.01$, Fig. 8E), suggesting that the mediation of CHE on the STAT3-regulated macrophage polarization might be related to the interaction with FBP1.

To further investigate the effect of FBP1 on M2 polarization and the STAT3 signaling pathway, siRNA was used to knock down FBP1 expression. The relative expression level of FBP1 was significantly reduced in the si-FBP1 group compared to the NC group, while no significant difference was observed between the M2 and NC groups ($P<0.01$, Fig. 9A). The expression levels of M2 polarization-related proteins, CD206 and Arg-1, were significantly downregulated in the si-FBP1 group compared to the NC group. Additionally, the si-FBP1+CHE group exhibited further reductions in CD206 and Arg-1 expression compared to the si-FBP1 group ($p < 0.05$ or $p < 0.01$, Fig. 9B). The expression levels of FBP1/STAT3-associated proteins were examined. FBP1 expression was significantly decreased in the si-FBP1 and si-FBP1+CHE groups relative to the NC group, with a further reduction observed in the si-FBP1+CHE group. Similarly, p-STAT3 levels were significantly reduced in the si-FBP1 group compared to the NC group, and the si-FBP1+CHE group showed an additional decrease relative to the si-FBP1 group. No significant changes were observed in STAT3 levels across groups($P<0.01$, Fig. 9C). These findings suggest that FBP1 plays a critical role in M2 polarization through the STAT3 signaling pathway, and its inhibition, particularly in combination with CHE treatment, significantly suppresses M2-associated protein expression and STAT3 activation.

Discussion

CHE, a primary bioactive alkaloid derived from *Chelidonium majus*, has shown promise in anti-BC research. While previous *in vitro* studies have demonstrated its direct antitumour effects on breast cancer (BC) cells, its *in vivo* efficacy and underlying mechanisms, particularly in modulating the TME, remain incompletely understood(Du et al., 2022). In this study, we established a 4T1 murine BC model and comprehensively investigated the impact of CHE on tumor progression, macrophage polarization, and the associated molecular mechanisms. Our *in vivo* experiments demonstrated that CHE treatment significantly inhibited tumor growth in BC mice. Notably, we observed that BC-bearing mice exhibited splenomegaly, which was alleviated after CHE administration. The spleen, a crucial immune organ, reflects immune status of the body, and the reduction in splenomegaly suggests that CHE may modulate the TME, potentially through immune regulation. These findings provide novel insights into the dual antitumour actions of CHE, which acts not only directly on tumour cells but also indirectly via immune modulation, which is a mechanism worthy of in-depth exploration.

The TME plays a paradoxical role in cancer therapy, functioning both as a facilitator and a barrier to treatment. Its diverse cellular components can promote tumour progression through the production pro-tumorigenic signals and immunosuppressive factors. TAMs are a predominant immune cell population within the TME and account for up to 25 % of infiltrating immune cells in treatment-naïve BC. TAMs, which can polarize into distinct phenotypes in response to microenvironmental cues, play a critical role in shaping the tumour-supportive landscape (Harris et al., 2024). TAMs typically display characteristics more akin to the M2-like phenotype and secrete protumorigenic factors such as IL-6, TGF-β, and Arg-1, which facilitate tumour growth, angiogenesis, and metastasis (Kundu et al., 2024).

Experimental validation confirmed that CHE treatment led to reduced expression of M2-associated markers such as CD206 and Arg-1 in both M2 macrophages and tumour tissues from BC-bearing mice. These results support the hypothesis that CHE may exert its anti-BC

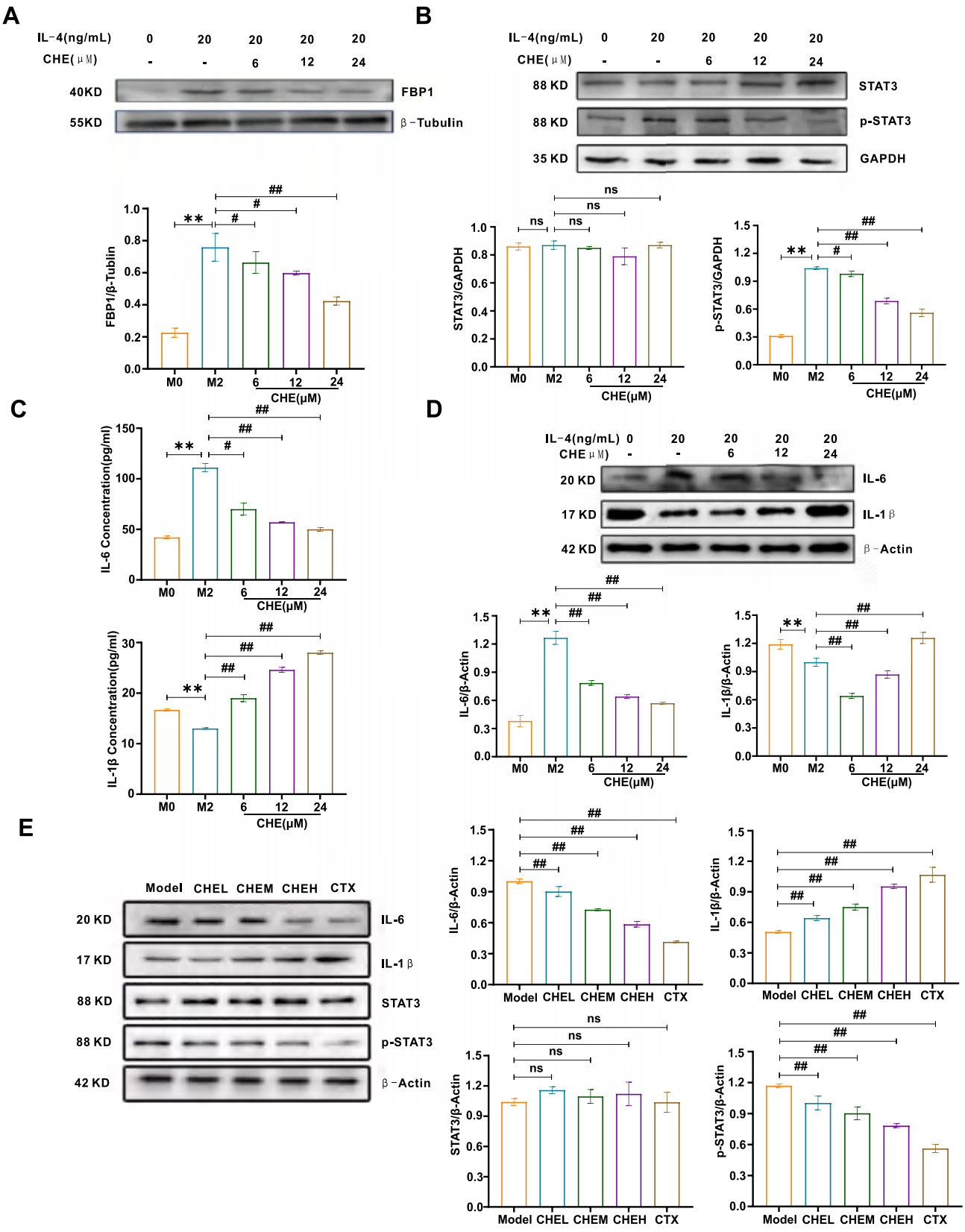

Fig. 8. Impact of CHE on the inhibition of macrophage M2 polarization via FBP1 - mediated regulation of the STAT3 pathway. (A) Expression of FBP1 protein in macrophages by western blot ($n = 3$). (B) Expression of STAT3 and p-STAT3 proteins in macrophages by western blot ($n = 3$). (C) Cytokine levels of IL-6 and IL-1β in macrophage supernatants by ELISA analysis ($n = 6$). (D) Expression of IL-6 and IL-1β proteins in macrophages by western blot ($n = 3$). (E) Expression of IL-6, IL-1β, STAT3, and p-STAT3 proteins in tumor tissue by western blot ($n = 3$). *$p < 0.05$, **$p < 0.01$ vs. the M0 group; #$p < 0.05$, ##$p < 0.01$ vs. the M2 group or the model group; ns, not significant.

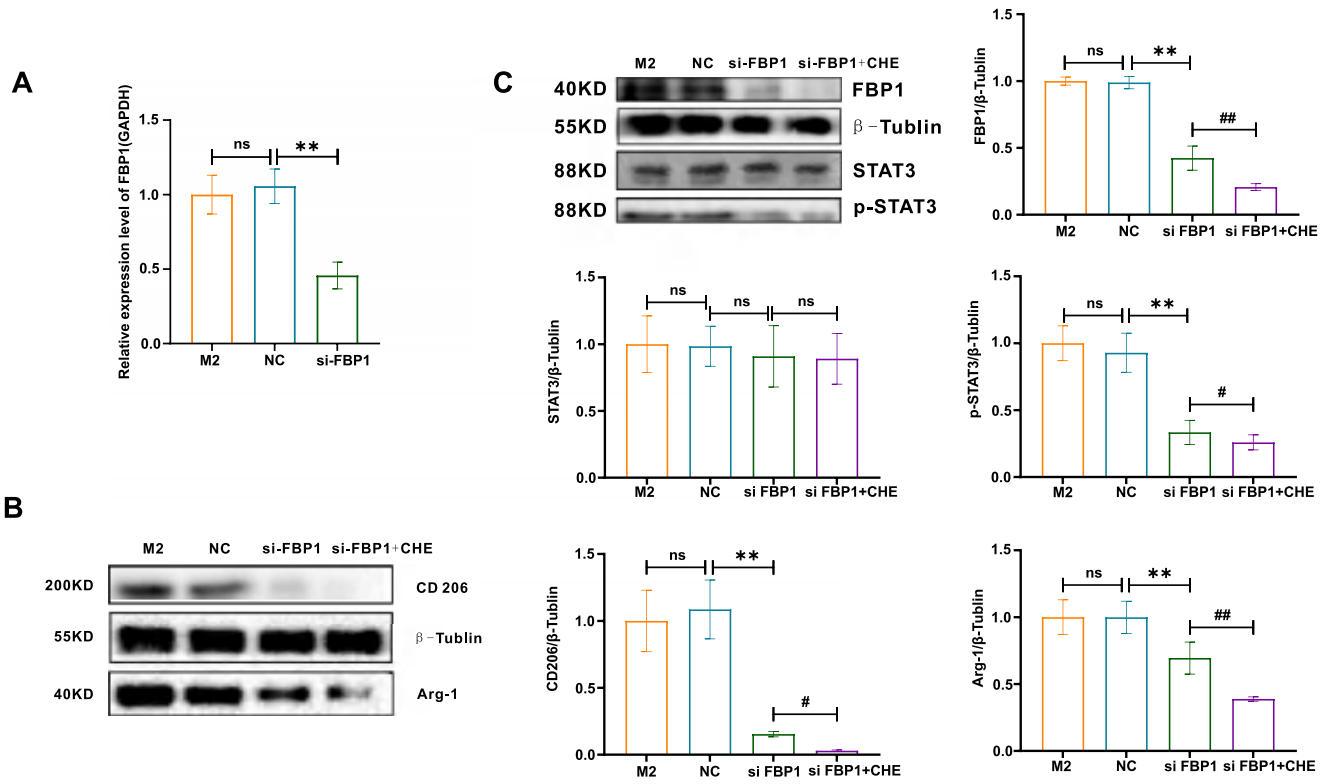

Fig. 9. Effects of FBP1 on M2 polarization and STAT3 signaling pathway (A) The expression level of FBP1 ($n = 3$). (B) The expression levels of M2 polarization-related proteins ($n = 3$). (C) The expression levels of FBP1/STAT3-associated proteins ($n = 3$). $^{*}p < 0.05$, $^{**}p < 0.01$ vs. the NC; $\#p < 0.05$, $\#\#p < 0.01$ vs. the siFBP1 group; ns, not significant.

effects by inhibiting M2-like macrophage polarization.

To further elucidate the mechanism by which CHE inhibits BC through suppression of M2 macrophage polarization, we used a coculture model of BC cells and macrophage-conditioned medium to simulate the influence of M2 macrophages within the TME. Our findings (Fig. 10) indicated that under coculture conditions, the anti-proliferative

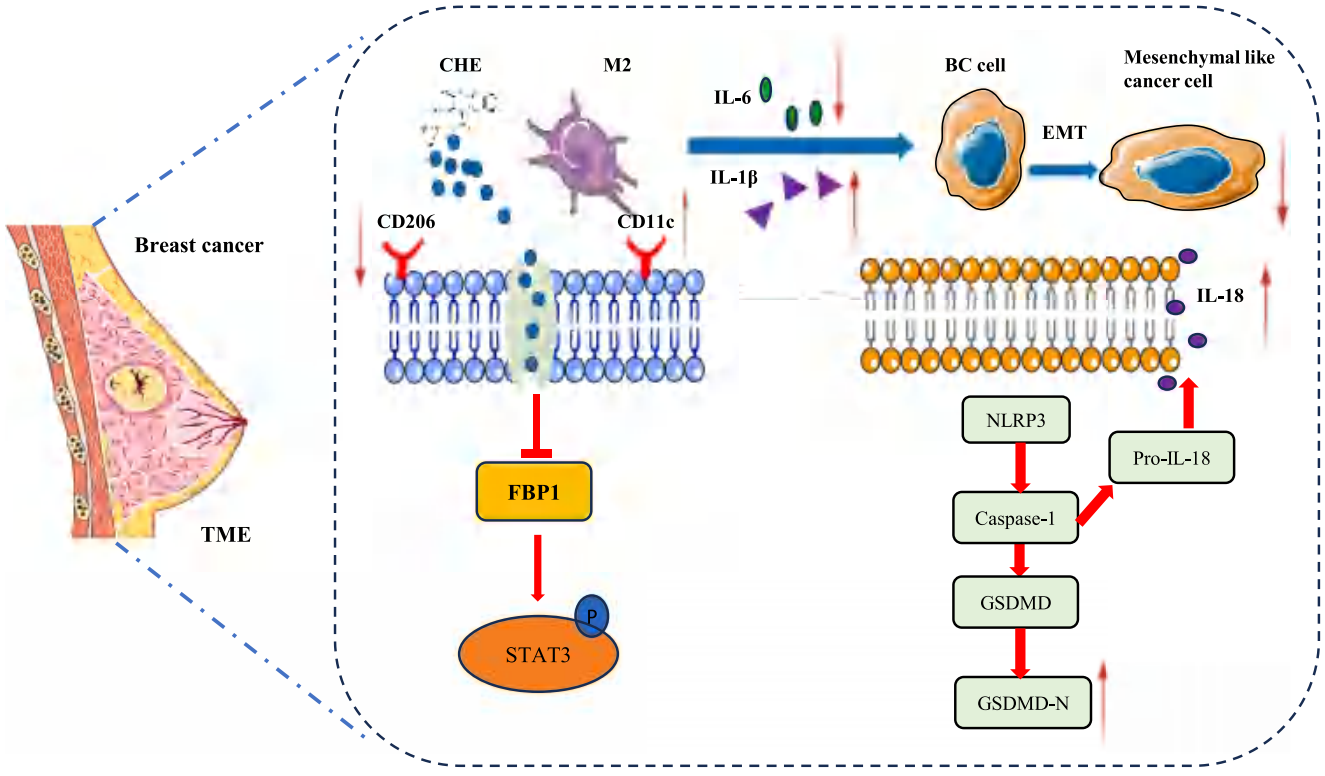

Fig. 10. Mechanism of CHE against breast cancer.

effect of CHE on BC cells may be mediated through the induction of pyroptosis. Pyroptosis is a highly inflammatory form of programmed cell death characterized by the activation of the NLRP3 inflammasome and its downstream effector GSDMD. This activation leads to the cleavage of GSDMD and the release of GSDMD-N, ultimately resulting in BC cell death (You et al., 2023). Pyroptotic markers, including cleaved caspase-1, GSDMD, and IL-18, were significantly upregulated in CHE-treated BC cells, and LDH release increased, confirming the induction of pyroptosis (Wang et al., 2023). Our findings indicate that following CHE treatment, 4T1 cells under coculture conditions exhibited increased LDH release, along with upregulated expression of GSDMD, GSDMD-N, IL-18, NLRP3, and cleaved caspase-1. We further investigated using the NLRP3 inhibitor MCC950 and found that blocking pyroptosis eliminated the effect of CHE on pyroptosis-related proteins. These findings suggest that within the M2 macrophage-induced TME, CHE induces pyroptosis in BC cells by compromising cell membrane integrity and activating the NLRP3/caspase-1/GSDMD signaling pathway.

Additionally, we investigated the mechanism by which CHE inhibits invasion and metastasis of BC cells under coculture conditions. Our results demonstrated that CHE markedly suppressed the migratory and invasive capabilities of BC cells, which may be associated with the inhibition of EMT. EMT is a critical process that facilitates cancer cell dissemination by enabling cancer cells to acquire mesenchymal-like properties, thereby enhancing their motility and invasiveness (Pouliquen et al., 2022). During EMT, downregulation of E-cadherin weakens cell–cell adhesion, whereas upregulation of N-cadherin enhances cell motility. Transcription factors such as Snail and Slug drive this transition by repressing E-cadherin expression, and MMP2 contributes to cell invasion by degrading the extracellular matrix, Together, drive the transition from an epithelial to a mesenchymal phenotype. Therefore, suppression of their expression indicates effective inhibition of EMT (Salehi et al., 2019). Moreover, in BC, VEGFA promotes tumour angiogenesis and induces the expression of EMT-related transcription factors such as Snail and Slug (Ronca et al., 2018). In this study, both *in vivo* and *in vitro* experiments demonstrated that CHE treatment upregulated the expression of E-cadherin but downregulated the expression of N-cadherin, MMP2, VEGFA, Snail, and Slug, indicating effective inhibition of EMT. These findings suggest that within the M2 macrophage-induced TME, CHE may exert its anti-invasion and anti-metastatic effects by suppressing EMT.

To further elucidate the mechanism by which CHE inhibits M2 macrophage polarization, a combination of network pharmacology, single-cell transcriptomics, and bulk transcriptomic analyses was employed. These integrative approaches identified FBP1 as a key regulatory target through whcih CHE inhibits M2 macrophage polarization. Molecular docking analysis revealed a strong binding affinity between CHE and FBP1, supporting the hypothesis that CHE may suppress M2 macrophage polarization by downregulating FBP1 expression. FBP1, a rate-limiting enzyme in gluconeogenesis, has recently been implicated in modulating the immune landscape of the TME. Elevated FBP1 expression in BC has been linked to increased levels of immunosuppressive factors (e.g., Arg-1, IL-10, and TGF-β), as well as an increased proportion of M2 macrophages, ultimately contributing to immune suppression (Sun et al., 2023). Western blot analysis revealed that FBP1 was highly expressed in M2 macrophages, and its expression was significantly reduced after CHE treatment. Further, knockdown of FBP1 in M2 macrophages using siRNA led to a significant decrease in the expression levels of M2 macrophage markers CD206 and Arg-1. Notably, the combination of siRNA knockdown and CHE treatment resulted in an even greater reduction in CD206 and Arg-1 expression levels. These findings suggest that FBP1 may play a critical role in the inhibitory effect of CHE on M2 macrophage polarization. Through both *in vitro* and *in vivo* studies, we demonstrated that CHE inhibits FBP1 expression, thereby suppressing M2 macrophage polarization.

Concurrently, our findings demonstrated that CHE enhanced STAT3 phosphorylation in macrophages, a modification known to inhibit M2 polarization. Phosphorylation of STAT3 upon IL-4 and IL-10 upregulated the expression of M2-associated genes such as Arg1 and CD206, representing a critical step in the induction of M2 polarization (Li Q., et al., 2022). Since it has been demonstrated that FBP1 exerts a key role in cancer immunoregulation by inhibiting STAT3-dependent PD-L1 expression (Wang et al., 2020), CHE may have modulated STAT3-dependent axis by targeting FBP1 to inhibit the M2 polarization of TAMs in the TME. The study found that CHE reduced STAT3 phosphorylation in M2 macrophages *in vitro*, decreased IL-6 levels, and increased IL-1β levels. A similar trend was observed in tumor tissues from mice. Furthermore, knockdown of FBP1 in M2 macrophages using siRNA also led to a reduction in STAT3 phosphorylation levels. These findings suggest that FBP1 may play a key role in M2 polarization through the STAT3 signaling pathway.

This study utilized the TNBC mouse model (4T1); however, significant differences in the immune microenvironment and metabolic pathways exist among various breast cancer subtypes. Therefore, further validation of CHE's effects in ER+ and HER2+ models is necessary to assess its broader therapeutic applicability. Additionally, while this study demonstrated that CHE targets FBP1 to regulate M2 macrophage polarization, the specificity of this interaction requires further confirmation. For clinical application, more research is needed to evaluate the pharmacokinetics, bioavailability, and potential toxicity of CHE to ensure its safety and efficacy in treating human breast cancer. Differences in immune systems, tumor heterogeneity, and metabolic characteristics between mouse models and human breast cancer further underscore the need for caution in translating these findings.

Future studies should explore the broader effects and mechanisms of CHE on other stromal cells, such as cancer-associated fibroblasts (CAFs), to comprehensively evaluate its role in modulating the tumor microenvironment (TME). Furthermore, while this study highlights the STAT3-FBP1 relationship in breast cancer, further investigation is warranted into the metabolic functions of FBP1, given its role as a key metabolic enzyme. Mechanistic studies on CHE's impact on FBP1-mediated metabolic regulation could provide deeper insights into its therapeutic potential. By addressing these aspects, future research could lay a strong foundation for the development of CHE as a novel and effective therapeutic strategy for breast cancer.

This study reveals a previously uncharacterized mechanism of CHE in breast cancer (BC) therapy, demonstrating significant novelty and innovation. For the first time, it confirms that CHE inhibits M2 macrophage polarization, highlighting its immunomodulatory role in suppressing tumor progression. While the anticancer effects of CHE have been reported, its regulatory impact on M2 macrophages had not been explored. Furthermore, the study employs single-cell transcriptomics and bulk transcriptomics analyses, integrated with network pharmacology, to identify FBP1 as a novel target. Experimental validation confirms the critical role of FBP1 in regulating M2 macrophage polarization.

CHE is proposed to inhibit FBP1 expression and STAT3 phosphorylation, potentially activating pyroptosis in breast cancer (BC) cells through the NLRP3/Caspase-1/GSDMD pathway. This mechanism may involve the reduction of IL-6 secretion by CHE, which could alleviate STAT3-mediated repression of NLRP3. Concurrently, CHE is hypothesized to induce apoptosis by suppressing the pro-survival STAT3/AKT signaling pathway. Together, these pathways may act in parallel to establish a coordinated "pro-death" state in BC cells, highlighting CHE's potential as an anti-tumor agent at the cellular level. In addition, CHE may indirectly inhibit epithelial-mesenchymal transition (EMT) by suppressing M2 macrophage polarization. M2 macrophages, key drivers of EMT within the tumor microenvironment (TME), secrete cytokines such as TGF-β and IL-6 that promote tumor invasion and metastasis. By targeting the FBP1/STAT3 axis, CHE is suggested to reduce M2 polarization and the secretion of these EMT-promoting factors, as evidenced in co-culture experiments and *in vivo* models (Fig. 10).

Conclusions

By integrating *in vivo* and *in vitro* experiments, the study validates CHE's impact on key M2 polarization markers and its ability to inhibit BC cell proliferation, migration, and invasion under coculture conditions. Furthermore, integrated analyses of network pharmacology, single-cell, and bulk RNA sequencing identify FBP1 as a novel molecular target of CHE, confirmed through molecular docking, Western blotting, and ELISA. CHE's regulation of the FBP1/p-STAT3 axis provides new insights into its immunosuppressive effects. These findings highlight CHE's potential as a novel therapeutic agent for BC and propose FBP1 as a promising target for cancer immunotherapy.

Ethics and consent

This research was conducted under approval and guidance of the Animal Ethics Committee of the School of Pharmacy, Harbin University of Commerce (Approval No. HSDYXY-2024032), issued on April 24, 2024.

Funding

This study was supported by the Heilongjiang Natural Science Foundation Joint Guidance Project (LH2022H001), "Outstanding Young Teachers' Basic Research Support Program" of Provincial Undergraduate Colleges and Universities in Heilongjiang Province (YQJH2024086), Fundamental Research Funds in Universities of Heilongjiang Province (2024-KYYWF-1018), "Spring Swallow" Support Program for Science and Technology Talent in Heilongjiang (CYCX24009) and Jixi "Challenge and Acceptance" Science and Technology Research Projects (JKJB2024H03), Graduate Student Innovative Research Program, Harbin University of Commerce (YJSCX2024-813HSD).

Data availability

All data were generated in-house, and no paper mill was used. All authors agree to be accountable for all aspects of work ensuring integrity and accuracy.

CRediT authorship contribution statement

Kaili Liu: Writing – review & editing, Methodology, Data curation. **Jianli Li:** Investigation, Data curation. **Zhiwei Sun:** Visualization. **Yuheng Sun:** Data curation. **Xuerui Zhang:** Investigation. **Yang Sui:** Methodology. **Zhongyuan Qu:** Supervision, Conceptualization. **Xiang Zou:** Supervision, Conceptualization.

Declaration of competing interest

The authors declare that they have no conflicts of interest.

Acknowledgements

We would like to express our heartfelt gratitude to Zhongjun Jiang, Ph.D. candidate at Northeast Forestry University, for providing invaluable guidance in bioinformatics analysis.

Supplementary materials

Supplementary material associated with this article can be found, in the online version, at doi:10.1016/j.phymed.2025.157451.

References

Aran, D., Looney, A.P., Liu, L., Wu, E., Fong, V., Hsu, A., Chak, S., Naikawadi, R.P., Wolters, P.J., Abate, A.R., Butte, A.J., Bhattacharya, M., 2019. Reference-based analysis of lung single-cell sequencing reveals a transitional profibrotic macrophage. Nat. Immunol. 20 (2), 163–172. https://doi.org/10.1038/s41590-018-0276-y.

Arnold, M., Morgan, E., Rumgay, H., Mafra, A., Singh, D., Laversanne, M., Vignat, J., Gralow, J.R., Cardoso, F., Siesling, S., Soerjomataram, I., 2022. Current and future burden of breast cancer: global statistics for 2020 and 2040. Breast 66, 15–23. https://doi.org/10.1016/j.breast.2022.08.010.

Barrett, T., Wilhite, S.E., Ledoux, P., Evangelista, C., Kim, I.F., Tomashevsky, M., Marshall, K.A., Phillippy, K.H., Sherman, P.M., Holko, M., Yefanov, A., Lee, H., Zhang, N., Robertson, C.L., Serova, N., Davis, S., Soboleva, A., 2013. NCBI GEO: archive for functional genomics data sets–update. Nucleic Acids Res. 41, D991–D995. https://doi.org/10.1093/nar/gks1193.

Chinese Pharmacopoeia Commission, 2025. Chinese Pharmacopoeia (2025 Edition), vol. IV. China Medical Science Press, Beijing.

Deepak, K.G.K., Vempati, R., Nagaraju, G.P., Dasari, V.R., S, N., Rao, D.N., Malla, R.R., 2020. Tumor microenvironment: challenges and opportunities in targeting metastasis of triple negative breast cancer. Pharmacol. Res. 153, 104683. https://doi.org/10.1016/j.phrs.2020.104683.

Du, S., Li, L., Gu, S., Cai, M., Li, X., 2022. Progress in the comprehensive research on pharmacological actions of celandine. Jilin J. Tradit. Chin. Med. 42, 84–87. https://doi.org/10.13463/j.cnki.jlzyy.2022.01.020.

Eberhardt, J., Santos-Martins, D., Tillack, A.F., Forli, S., 2021. AutoDock Vina 1.2.0: new docking methods, expanded force field, and python bindings. J. Chem. Inf. Model. 61 (8), 3891–3898. https://doi.org/10.1021/acs.jcim.1c00203.

Elhanani, O., Ben-Uri, R., Keren, L., 2023. Spatial profiling technologies illuminate the tumor microenvironment. Cancer Cell 41, 404–420. https://doi.org/10.1016/j.ccell.2023.01.010.

Ernst, E., Schmidt, K., 2005. Ukrain - a new cancer cure? A systematic review of randomised clinical trials. BMC Cancer 5, 69. https://doi.org/10.1186/1471-2407-5-69.

Gou, L., Yue, G.G., Puno, P.T., Lau, C.B., 2021. A review on the relationship of mast cells and macrophages in breast cancer - Can herbs or natural products facilitate their anti-tumor effects? Pharmacol. Res. 164, 105321. https://doi.org/10.1016/j.phrs.2020.105321.

Hao, Y., Stuart, T., Kowalski, M.H., Choudhary, S., Hoffman, P., Hartman, A., Srivastava, A., Molla, G., Madad, S., Fernandez-Granda, C., Satija, R., 2024. Dictionary learning for integrative, multimodal and scalable single-cell analysis. Nat. Biotechnol. 42, 293–304. https://doi.org/10.1038/s41587-023-01767-y.

Harris, M.A., Savas, P., Virassamy, B., O'Malley, M.M.R., Kay, J., Mueller, S.N., Mackay, L.K., Salgado, R., Loi, S., 2024. Towards targeting the breast cancer immune microenvironment. Nat. Rev. Cancer 24, 554–577. https://doi.org/10.1038/s41568-024-00714-6.

He, Z., Hu, Y., Zhang, Y., Xie, J., Niu, Z., Yang, G., Zhang, J., Zhao, Z., Wei, S., Wu, H., Hu, W., 2024. Asiaticoside exerts neuroprotection through targeting NLRP3 inflammasome activation. Phytomedicine 127, 155494. https://doi.org/10.1016/j.phymed.2024.155494.

Hou, F.J., Guo, L.X., Zheng, K.Y., Song, J.N., Wang, Q., Zheng, Y.G., 2019. Chelidonine enhances the antitumor effect of lenvatinib on hepatocellular carcinoma cells. Oncotargets Ther. 12, 6685–6697. https://doi.org/10.2147/OTT.S215103.

Hu, C., Li, T., Xu, Y., Zhang, X., Li, F., Bai, J., Chen, J., Jiang, W., Yang, K., Ou, Q., Li, X., Wang, P., Zhang, Y., 2023. CellMarker 2.0: an updated database of manually curated cell markers in human/mouse and web tools based on scRNA-seq data. Nucleic Acids Res. 51 (D1), D870–D876. https://doi.org/10.1093/nar/gkac947.

Jang, H.J., Yang, J.H., Hong, E., Jo, E., Lee, S., Lee, S., Choi, J.S., Yoo, H.S., Kang, H., 2021. Chelidonine induces apoptosis via GADD45a-p53 regulation in human pancreatic cancer cells. Integr. Cancer Ther. 20, 15347354211006191. https://doi.org/10.1177/15347354211006191.

Kim, S., 2016. Getting the most out of PubChem for virtual screening. Expert Opin. Drug Discov. 11, 843–855. https://doi.org/10.1080/17460441.2016.1216967.

Kundu, M., Butti, R., Panda, V.K., Malhotra, D., Das, S., Mitra, T., Kapse, P., Gosavi, S.W., Kundu, G.C., 2024. Modulation of the tumor microenvironment and mechanism of immunotherapy-based drug resistance in breast cancer. Mol. Cancer 23, 92. https://doi.org/10.1186/s12943-024-01990-4.

Li, H., Tang, X., Sun, Z., Qu, Z., Zou, X., 2024. Integrating bioinformatics and experimental models to investigate the mechanism of the chelidonine-induced mitotic catastrophe via the AKT/FOXO3/FOXM1 axis in breast cancer cells. Biomol. Biomed. 24, 560–574. https://doi.org/10.17305/bb.2023.9665.

Li, J., Wang, S., Wang, N., Zheng, Y., Yang, B., Wang, X., Zhang, J., Pan, B., Wang, Z., 2021. Aiduqing formula inhibits breast cancer metastasis by suppressing TAM/CXCL1-induced Treg differentiation and infiltration. Cell Commun. Signal. 19, 89. https://doi.org/10.1186/s12964-021-00775-2.

Li, Q., Cheng, Y., Zhang, Z., Bi, Z., Ma, X., Wei, Y., Wei, X., 2022. Inhibition of ROCK ameliorates pulmonary fibrosis by suppressing M2 macrophage polarisation through phosphorylation of STAT3. Clin. Transl. Med. 12, e1036. https://doi.org/10.1002/ctm2.1036.

Nowicky, J.W., Staniszewski, A., Zbroja-Sontag, W., Slesak, B., Nowicky, W., Hiesmayr, W., 1991. Evaluation of thiophosphoric acid alkaloid derivatives from *Chelidonium majus* L. ("Ukrain") as an immunostimulant in patients with various carcinomas. Drugs Exp. Clin. Res. 17, 139–143.

Pal, B., Chen, Y., Vaillant, F., Capaldo, B.D., Joyce, R., Song, X., Bryant, V.L., Penington, J.S., Di Stefano, L., Tubau Ribera, N., Wilcox, S., Mann, G.B., , kConFab, Papenfuss, A.T., Lindeman, G.J., Smyth, G.K., Visvader, J.E., 2021. A single-cell RNA expression atlas of normal, preneoplastic and tumorigenic states in the human breast. EMBO J. 40 (11), e107333. https://doi.org/10.15252/embj.2020107333.

Panzer, A., Hamel, E., Joubert, A.M., Bianchi, P.C., Seegers, J.C., 2000. Ukrain(TM), a semisynthetic *Chelidonium majus* alkaloid derivative, acts by inhibition of tubulin

polymerization in normal and malignant cell lines. Cancer Lett. 160, 149–157. https://doi.org/10.1016/s0304-3835(00)00578-4.
Park, M., Kim, D., Ko, S., Kim, A., Mo, K., Yoon, H., 2022. Breast cancer metastasis: mechanisms and therapeutic implications. Int. J. Mol. Sci. 23, 6806. https://doi.org/10.3390/ijms23126806.
Pouliquen, D.L., Boissard, A., Henry, C., Coqueret, O., Guette, C., 2022. Curcuminoids as modulators of EMT in invasive cancers: a review of molecular targets with the contribution of malignant mesothelioma studies. Front. Pharmacol. 13, 934534. https://doi.org/10.3389/fphar.2022.934534.
Qu, Z., Li, H., Qiang, F., Liu, K., Wu, S., Li, J., Zou, X., 2025. Regulation of inflammation by Chaihu-Shugan-San: targeting the IL-17/NF-κB pathway to combat breast cancer-related depression. Phytomedicine 143, 156836. https://doi.org/10.1016/j.phymed.2025.156836.
Ronca, R., Van Ginderachter, J.A., Turtoi, A., 2018. Paracrine interactions of cancer-associated fibroblasts, macrophages and endothelial cells: tumor allies and foes. Curr. Opin. Oncol. 30, 45–53. https://doi.org/10.1097/CCO.0000000000000420.
Ru, J., Li, P., Wang, J., Zhou, W., Li, B., Huang, C., Li, P., Guo, Z., Tao, W., Yang, Y., Xu, X., Li, Y., Wang, Y., Yang, L., 2014. TCMSP: a database of systems pharmacology for drug discovery from herbal medicines. J. Cheminform. 6, 13. https://doi.org/10.1186/1758-2946-6-13.
Salehi, B., Varoni, E.M., Sharifi-Rad, M., Rajabi, S., Zucca, P., Iriti, M., Sharifi-Rad, J., 2019. Epithelial-mesenchymal transition as a target for botanicals in cancer metastasis. Phytomedicine 55, 125–136. https://doi.org/10.1016/j.phymed.2018.07.001.
Schake, P., Bolz, S.N., Linnemann, K., Schroeder, M., 2025. PLIP 2025: introducing protein-protein interactions to the protein-ligand interaction profiler. Nucleic Acids Res. 53 (W1), W463–W465. https://doi.org/10.1093/nar/gkaf361.
Sun, H., Zhang, H., Jing, L., Zhao, H., Chen, B., Song, W., 2023. FBP1 is a potential prognostic biomarker and correlated with tumor immunosuppressive microenvironment in glioblastoma. Neurosurg. Rev. 46, 187. https://doi.org/10.1007/s10143-023-02097-y.
Tang, Z., Kang, B., Li, C., Chen, T., Zhang, Z., 2019. GEPIA2: an enhanced web server for large-scale expression profiling and interactive analysis. Nucleic Acids Res. 47, W556–W560. https://doi.org/10.1093/nar/gkz430.
Consortium, UniProt, 2023. UniProt: the Universal Protein Knowledgebase in 2023. Nucleic Acids Res. 51, D523–D531. https://doi.org/10.1093/nar/gkac1052.
Waks, A.G., Winer, E.P., 2019. Breast cancer treatment: a review. JAMA 321, 288–300. https://doi.org/10.1001/jama.2018.19323.
Wang, B., Zhou, Y., Zhang, J., Jin, X., Wu, H., Huang, H., 2020. Fructose-1,6-bisphosphatase loss modulates STAT3-dependent expression of PD-L1 and cancer immunity. Theranostics 10, 1033–1045. https://doi.org/10.7150/thno.38137.
Wang, J.L., Hua, S.N., Bao, H.J., Yuan, J., Zhao, Y., Chen, S., 2023. Pyroptosis and inflammasomes in cancer and inflammation. MedComm 4, e374. https://doi.org/10.1002/mco2.374.
Xie, Y.J., Gao, W.N., Wu, Q.B., Yao, X.J., Jiang, Z.B., Wang, Y.W., Wang, W.J., Li, W., Hussain, S., Liu, L., Leung, E.L., Fan, X.X., 2020. Chelidonine selectively inhibits the growth of gefitinib-resistant non-small cell lung cancer cells through the EGFR-AMPK pathway. Pharmacol. Res. 159, 104934. https://doi.org/10.1016/j.phrs.2020.104934.
You, H.M., Wang, L., Meng, H.W., Huang, C., Fang, G.Y., Li, J., 2023. Pyroptosis: shedding light on the mechanisms and links with cancers. Front. Immunol. 14, 1290885. https://doi.org/10.3389/fimmu.2023.1290885.
Yu, R., 2010. Commonly Used Antitumor Drug Pairs by Yu Rencun. People's Medical Publishing House, Beijing.
Zou, X., Wang, Y.M., Wang, J.Q., Long, L.L., Wang, C., Liu, Y., Sheng, J.J., Qu, Z.Y., 2014. Research progress on pharmacological activities of chelidonine. J. Mod. Clin. Med. 29, 1326–1330.
Zou, X., Zhang, Y., Liu, K., Zhang, L., Li, J., Zhang, Y., Zhang, X., Yu, L., Qu, Z., 2025a. Chelidonine overcomes p-gp-mediated adriamycin resistance in mcf-7/adr cells by inhibiting pdgfrβ/pi3k/akt pathway. Chin. Herb. Med. 17, 123–134. https://doi.org/10.1016/j.chmed.2025.01.005.